Interaction of transmutation products with precipitates, dislocations and grain boundaries in neutron irradiated W

M.J. Lloyd [a,b,c,*], A.J. London [c], J.C. Haley [b,c], M.R. Gilbert [c], C.S. Becquart [d,f], C. Domain [d,e], E. Martinez [g,h], M.P. Moody [b], P.A.J. Bagot [b], D. Nguyen-Manh [b,c], D.E.J. Armstrong [b]

[a] Engineering Product Development, Singapore University of Technology and Design, 8 Somapah Rd, Singapore 487372
[b] Department of Materials, University of Oxford, Parks Road, Oxford OX1 3PH, UK
[c] Culham Centre for Fusion Energy, United Kingdom Atomic Energy Authority, Culham, Abingdon, Oxfordshire OX14 3DB, UK
[d] Univ. Lille, CNRS, INRAE, Centrale Lille, UMR 8207-UMET-Unité Matériaux et Transformations, Lille F-59000, France
[e] Laboratoire commun EDF-CNRS Etude et Modélisation des Microstructures pour le Vieillissement des, Matériaux (EM2VM), France
[f] EDF-R&D, Département Matériaux et Mécanique des Composants (MMC), Les Renardières, Moret sur Loing Cedex, F-77818, France
[g] Department of Mechanical Engineering, Clemson University, Clemson, SC 29634, USA
[h] Department of Materials Science and Engineering, Clemson University, Clemson, SC 29634, USA

ARTICLE INFO

ABSTRACT

Tungsten is the primary candidate materials for the high neutron flux, high temperature components of a future demonstration fusion reactor. Despite this, there is a lack of data on W under fusion relevant neutron doses and irradiation temperatures. In this study, single crystal and polycrystalline W samples irradiated at the High Flux Reactor (HFR) at 900 °C were characterised using Atom Probe Tomography (APT) and Scanning Transmission Electron Microscopy (STEM). Bulk chemical and isotopic concentration predictions were validated by analysing the mass spectrum from APT experiments. A post irradiation composition of W-1.26 ± 0.15 at.%Re - 0.08 ± 0.02 at.%Os - 0.01 ± 0.01 at.%Ta was measured in the single crystal sample, whereas W-1.09 ± 0.07 at.%Re - 0.08 ± 0.02 at.%Os - 0.01 ± 0.01 at.%Ta was measured for the polycrystalline. APT and STEM showed that a high number density of Re and Os rich precipitates had formed under neutron irradiation. These typically consisted of a core rich in Re and Os, surrounded by a less dense Re rich cloud. Multiple analysis methods were applied to investigate the composition of these clusters. APT showed that the centres of some of the precipitates had a rod shaped core which were rich in both Re and Os. Line profile analysis suggests that in the centre of the precipitates, the threshold composition for σ phase formation may have been reached, as has been observed in higher transmutation rate experiments. In addition, dislocations, sub grain boundaries and dislocation loops were all shown to be decorated with both Re and Os, in agreement with predictions from DFT simulations.

1. Introduction

Understanding the interaction between neutron induced transmutation products and microstructural features such as dislocations and grain boundaries is vital for the development of reliable components for both a demonstration fusion power station (DEMO). Transmutation of elements in reactor components leads to the production of light elements (such as H and He) and elements adjacent the parent in the periodic table, through a sequence of neutron reactions and subsequent nuclide decays. For materials such as tungsten, which has a relatively high cross section for neutron absorption reactions [1,2], transmutation to the adjacent elements is significant [3,4], and results in components which have a strongly time dependant chemical composition [3]. Transmuta-

tion reactions are also most significant in the high neutron flux regions of the reactor where the deployment of W is envisaged, such as in the first wall (FW) and divertor regions which together make up the plasma facing components (PFCs).

W has a number of attractive properties which make it the primary candidate for use in the PFCs, including a comparatively low induced long-term activity after neutron irradiation (in pure form [5]), a high melting temperature (3695 K [6]), good thermal conductivity (165 Wm^{-1} K^{-1} at room temperature [7]) and a high resistance to sputtering under H/He plasma exposure [8]. Tungsten is not a commonly used engineering material within the nuclear industry because of its inherently poor mechanical properties (Ductile-to-Brittle Transition Temperature (DBTT) ≈623–723 K [9,10] and brittle behaviour at room tem-

perature [11]), its tendency to undergo inter-granular fracture [12,13], and due to difficulties in its forming. Furthermore, neutron irradiation of W has been linked to a significant degradation in thermal and mechanical properties. A shift in the DBTT of between 500 and 1000 K has been observed in neutron irradiated tungsten from the HFR and BR2 reactors [9,14]. Both nanoindentation and microindentation have been also used to measure irradiation induced hardening in ion implanted samples [15–20], and in neutron irradiated samples from various fission spectrum reactors [21–26]. The change in thermal diffusivity of W is another important factor which could limit the lifetime of the PFCs, and a number of studies have measured a significant decrease following neutron [23] and ion irradiation [27,28]. The production of solute elements through transmutation, and subsequent radiation-induced precipitation, is one of the key contributors to the degradation of these properties under neutron irradiation, along with the formation of dislocation loops and voids [21].

In W, transmutation leads to the production of Re and Os, through a sequence of (n, γ) neutron absorption reactions and β^- decays. Ta is also produced primarily via the β^+ decay of isotopes which have undergone $(n, 2n)$ neutron loss reactions [29]. The amount of transmutation is strongly dependant on the incident neutron energy spectrum, with lower energy neutrons having a higher cross section for absorption. This makes comparison between samples irradiated at different reactors very difficult, as there are major differences in the neutron energy spectrum caused by the design of the reactor, the presence of adjacent samples and the physical location of the samples within the reactor core. However, on average, reactors with a higher proportion of thermal neutrons generate samples with transmutation levels significantly greater than is expected for a DEMO reactor, per unit of damage in displacements per atom (dpa). For more information on the calculation of dpa, the reader is referred to Nordlund et al. [30], 31]. Reactors with a high proportion of fast neutrons, or experiments in which the thermal neutron population has been decreased through canister design, generate a smaller quantity of transmutation products per dpa of damage [22,32], but still significantly higher than is expected for a DEMO reactor [3]. Even at DEMO transmutation levels, the W components the reactor are expected to generate a significant quantity of Re and Os during their lifetime [4,29,33,34]. The presence of Ta is not thought to have a major detrimental impact on mechanical properties [17].

Alloying W with Re (up to a maximum of around 8 at.%Re) is known to reduce the DBTT [12,35–38] and results in a decrease in hardness [35]. Increasing the Re content further results in an increase in hardness which is associated with the formation of the brittle, intermetallic σ-phase (WRe) [35]. Under irradiation the benefits of Re alloying are reversed due to radiation induced segregation of Re. Studies between the 1960s and 1980s were performed on neutron irradiated W-Re alloys [35–38]. Subsequent studies focused on the irradiation of pure W samples, as its application within the PFCs of a fusion reactor was explored. Neutron irradiation of pure W samples at the EBR-II reactor led to the observation of the Re rich χ phase (WRe$_3$), rather than the expected σ phase [39]. In subsequent studies a mixture of σ or χ phase has been reported [40]. Transmission Electron Microscopy (TEM) and Scanning Transmission Electron Microscopy (STEM) analysis of these precipitates generally find a needle or rod shaped morphology. Microstructural characterisation of samples from various reactors have found a combination of dislocation loops, voids and Re rich precipitates, the ratio of which depends on the irradiation temperature and dose. At higher doses where Re and Os production is significant, the hardening response is primarily caused by these Re rich precipitates [21].

Atom Probe Tomography (APT) analysis of samples irradiated in experiments with comparatively low transmutation rates found Re rich clusters, rather than precipitates consistent with either σ or χ phase [32]. APT analysis of samples from HFIR with higher levels of transmutation have found needle shaped precipitates that have contain approximately 20 at.%Re and 13 at.%Os [41]. STEM-EDX analyses performed on samples irradiated at the BR2 reactor, producing relatively low trans-

mutation rates, found clear evidence for both σ and χ phase, including evidence for an Os rich, intermetallic χ phase (WOS$_3$) [40], which is not present in the binary W-Os phase diagram [42,43].

Ion irradiation does not induce transmutation reactions, and has been carried out in pure-W, W-Re, W-Re-Ta and W-Re-Os alloys [15–17,20,44]. In general Re and Os clustering has been consistently observed using APT, but not the formation of phases with a composition consistent with either the σ or χ phase.

Computational studies suggest that kinetic transport of Re, via mixed-interstitial dumbbell mediated migration is responsible for the observed precipitation of Re, well below the expected solubility limit [45,46]. However, these studies focus on binary W-Re, and do not fully account for void formation. The impact of Os on the microstructure is less clear, but DFT modelling suggests that Os may play a more significant role than Re, due to its stronger binding with point defects. Os was also found to decorate dislocations in APT of unirradiated W-Os in 1983 by Eaton and Norden [47]. Xu et al. observed that Os had a strong impact on the cluster structure, with the addition of 1 at.%Os acting to suppress Re clustering, by preferentially forming small Os rich clusters [16].

In this study, neutron irradiated W samples from the HFR reactor are studied with the overarching aim of understanding the distribution and location of the primary transmutation products, rhenium and osmium, with respect to both the pre-existing defects, such as grain boundaries; and irradiation induced defects such as dislocation loops and clusters of transmutation atoms. Microstructural analysis is performed using a combination of APT and STEM - High Angle Annular Dark Field (HAADF) imaging. These complementary techniques were used to investigate the different distribution of microstructural features, as well as the concentrations of Re and Os transmutation products. This approach allows for a better understanding of the sensitivities of each technique to different features. In several previous studies of similar ion and neutron irradiated W samples, only a single imaging method has been used to study microstructural evolution, which can lead to unintentional misrepresentations of the dominant features observed. Furthermore, computational modelling of microstructural evolution under neutron irradiation requires a full understanding of the influence of the various features on the behaviour of Re and Os atoms produced by transmutation. The objectives of this study were therefore as follows:

1. APT will be used to analyse the microstructure of both single crystal and polycrystalline material, to analyse the structure of the precipitates which are formed. The composition of the clusters will be measured to determine whether they are consistent with the formation of σ or χ phases that are seen in other low transmutation rate neutron irradiation experiments.
2. The number densities of different microstructural features such as voids, loops and precipitates will be investigated using STEM-HAADF imaging. This will be compared to the number densities of precipitates given by APT. Characterising the number densities of these features will give a better understanding of the observed differences between samples with comparable irradiation conditions.
3. The interaction of transmutation products with grain boundaries and dislocation loops will be investigated by using targeted APT. Density Functional Theory (DFT) modelling of dislocation loops in W will be used to support the observed segregation of Re/Os to these features.

2. Methodology

2.1. Samples and neutron irradiation

The samples used in this study were irradiated between 2008 and 2009 as part of the ExtreMat-II programme at the High Flux Reactor (HFR) in Petten, Netherlands. Samples of commercially pure single crystal and polycrystalline W were purchased from Metal Crystals and Oxides Limited, Cambridge UK (no longer trading). The samples were
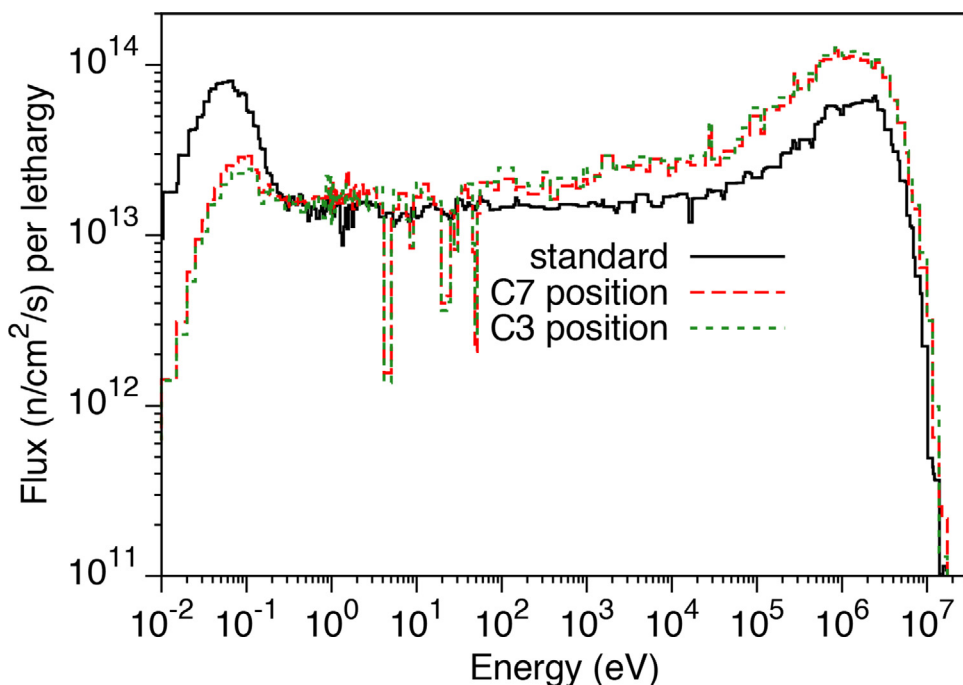
Fig. 1. Local neutron energy spectrum received by samples in the two reactor locations in HFR (C7 and C3), overlaid over the averaged neutron energy spectrum for the reactor.

100 mm long rods, 10 mm in diameter. The polycrystalline sample had a fine grained microstructure dominated by elongated grains oriented along the rolling direction. Previous analysis of these samples showed that there was an average grain size of 100×10 um with sub grains approximately 20×2 um [48]. The samples were polished using a series of successively finer SiC grit papers, diamond suspension paste diluted with water (6 um, 3 um and 1 um) and finally using colloidal silica. The samples were then annealed at 1673 K for 24 h.

The samples underwent neutron irradiation at HFR, starting in 2008. Technical problems resulted in neutron irradiation being stopped in the summer of 2008, and resumed in the spring of 2009. Irradiation ended in April 2009. The samples were loaded alongside others into the HFR reactor and received a 208 full power day irradiation in 2 locations at 1173 K. The specimen temperature was controlled during irradiation using a gas-mixture technique. The samples were located in positions C7 and C3 in drums 3 and 4. In total the samples received a neutron fluence of 1.21×10^{26} m^{-2} (6.5×10^{25} m^{-2} at an energy above 1×10^{-1} MeV): 6.8×10^{18} m^{-2} s^{-1} in the first location and 6.6×10^{18} m^{-2} s^{-1} in the second location. The presence of an adjacent, strong thermal neutron absorber caused local modification of the neutron energy spectrum, reducing the thermal neutron population, as shown in Fig. 1. Following irradiation the samples had a specific activity of 8.2 MBqkg^{-1} after 5 years of cooling.

The dose in dpa received by the sample and the transmutation level were quantified via nuclear inventory modelling using FISPACT-II [49], in simulations carried out using a displacement threshold energy of 55 eV. The simulations used the TENDL-2015 [50] nuclear cross section data library and accounted for self-shielding effects in the material using appropriate probability tables (see [29] for details), and also included the impact of the two different locations (C7 and C3) within the reactor via appropriate use of the local energy spectrum (Fig. 1). The simulations were performed for the 208 days of exposure and 6 years of decay following removal from the reactor [32,51].

A total dose of 1.67 dpa and a post-irradiation composition of 1.4 at.%Re - 0.1 at.%Os - 0.02 at.%Ta was predicted. This composition was experimentally verified by Abernethy et al. using γ-ray spectroscopy of the ^{186}Re decay and SEM-EDX measurements [9,48,51], and by Lloyd et al. using APT [32]. Both EDX and APT of the single crystal sample

Table 1

Bulk sample solute concentration from transmutation measured using APT with an uncertainty quantified using mass-to-charge peak under and over ranging approach, details of which are given in Lloyd et al. [32]. Also given is the FISPACT-II results [32] and EDX measurements from these samples [9].

Sample	Re (at.%)	Os (at.%)	Ta (at.%)
Single Crystal	1.26 ± 0.15	0.08 ± 0.02	0.01 ± 0.01
Polycrystalline	1.09 ± 0.07	0.08 ± 0.02	0.01 ± 0.01
FISPACT-II	1.4	0.1	0.02
EDX [9]	1.2	0.1	Undetectable

showed good agreement with the FISPACT-II modelling (as shown in Table 1).

2.2. Post-irradiation sample preparation

APT relies on the fabrication of sharp needle shaped samples in order to maximise the evaporation field at the tip. In this research, a Focused Ion Beam (FIB) liftout technique was used to prepare site specific and bulk samples. FIB work was carried out remotely in hot cell facilities at the Materials Research Facility (MRF), United Kingdom Atomic Energy Authority (UKAEA), using an FEI Helios dual beam FIB-SEM system. The calculated activity from an individual lift-out was <1 Bq which allowed for non-active APT/TEM analysis in facilities at the David Cockayne Centre for Electron Microscopy (DCCEM), and Research Group in Atom Probe Tomography at Oxford Department of Materials.

The cantilever was removed from the sample surface using an Omniprobe micromanipulator and cross sections were mounted onto silicon posts on a 22 grid coupon, using Pt deposition. An initial electron beam deposited Pt layer was used to protect the sample surface during subsequent ion beam Pt deposition. The samples were sharpened into needles using a series of successively smaller annular milling patterns and lower beam currents (1.5 nA - 40 pA) and an acceleration voltage of 30 kV. At a tip diameter of between approximately 50–100 nm in diameter, a final polishing stage using an acceleration voltage of 2 kV and a beam current

of 300 pA was used to remove approximately 500 nm of Ga implanted material from the top of the needle.

Targeted APT was performed on grain boundaries of the polycrystalline sample, using a site-specific FIB lift-out procedure. The boundary of a grain was chosen (the size of which indicated that it was a sub-grain boundary) and a protective layer of Pt was deposited using the procedure outlined above. The grain boundary was positioned centrally within the needle during sharpening, using the contrast between adjacent grains in the electron and ion images. The GB was positioned so that it was within the top 100–300 nm of the tip. As the thickness of the tip was reduced, the contrast between the adjacent grains became weaker. Therefore, when the GB was within approximately 500 nm of the apex, a 2 kV polishing stage was applied until the distance between the GB and the apex of the tip was removed from the sample.

2.3. Atom probe tomography

APT was carried out in a CAMECA LEAP 5000 XR at the University of Oxford in laser-assisted mode, using a sample temperature of 55 K, a laser pulse energy of 80–125 pJ and a pulse frequency of 100–200 kHz. A medium sensitivity fast emission control (FEC) setting, with a voltage step of 5% was used in order to mitigate against sudden increases in ion evaporation observed during the evaporation of a Re rich area. Parameters were chosen primarily to increase the yield of data from each specimen, as a high sample fracture rate occurred in both single crystal and polycrystalline samples. The highest rate of failure was in the polycrystalline samples.

In total, 10 samples were obtained from the single crystal sample giving a total count of 2.141×10^7 ranged ions. For the polycrystalline sample, 2 samples containing a section of a grain boundary were obtained, and 4 without grain boundaries, with a total count of 1.371×10^7 ions. The data was reconstructed and visualised using IVAS 3.8.2, using a under/over peak ranging method described in a previous publication [32]. Reconstructions were carried out using a tip radius estimated by the voltage curve in IVAS as an input, unless specified otherwise. The mass spectra of multiple APT data sets were analysed using the CompositionFromPosList.m Matlab script in the AtomProbeLab software package [52].

2.4. Density functional theory calculations

DFT calculations were done within the projector augmented wave (PAW) method as implemented in the Vienna ab initio simulation package VASP [53,54]. The exchange-correlation functional is described by the generalized gradient approximation (GGA) of PBE [55]. For the self interstitial atom (SIA) loop calculations, 1458 bcc positions supercells were used with Gamma point representation of the Brillouin zone (referred to as 1 kpt calculations). A selected number of configurations were also calculated using $2 \times 2 \times 2$ kpoints. All atomic relaxations were performed under constant volume condition. A perfect $1/2 \langle 111 \rangle$ loop containing 37 SIA has been introduced in the middle of the supercell and the binding energy of different solute atoms determined for various positions of the solute. The formation $1/2 \langle 111 \rangle$ dislocation loops undergoing quantum mechanical one-dimensional glide diffusion in irradiated tungsten has been discussed recently from both experimental and theoretical points of view [56]. The influence of the pressure due to the use of constant volumes has been evaluated using the method proposed by Varvenne et al.[57] to take into account long range interactions. Once point defect energies have been calculated using VASP, they are corrected by subtracting artificial interaction energy arising from periodic boundary conditions. The calculations were done using the minimal set regular PAW which considers s and d electrons as valence electrons. We estimated the error for not taking into account the semi-core states and only 1 kpt to be around 0.1 eV, the uncertainty being always the highest for Os and Ta.

Table 2

Comparison between the calculated distribution of isotopes and the measured distribution from APT produced by transmutation as a percentage of the total number of atoms in the simulation and the total number of ranged ions in APT. The 11 most commonly occurring isotopes from the simulation are included, isotopes with lower concentration could not be separated from background using APT. Uncertainty on the concentration from APT is estimated by comparing different ranging approaches, background-to-background and at FWHM.

Isotope	FISPACT-II (at.%)	Single crystal (at.%)	Poly-crystalline bulk (at.%)
^{184}W	30.97	31.9 ± 0.9	31.9 ± 1.1
^{186}W	26.99	26.1 ± 0.8	26.6 ± 0.3
^{182}W	25.35	24.8 ± 0.6	24.1 ± 1.3
^{183}W	15.02	15.4 ± 0.6	15.0 ± 0.5
^{187}Re	1.34	1.24 ± 0.06	1.03 ± 0.05
^{188}Os	0.10	0.08 ± 0.02	0.08 ± 0.03
^{180}W	0.10	0.11 ± 0.01	0.08 ± 0.01
^{185}Re	0.09	0.11 ± 0.01	0.11 ± 0.01
^{181}Ta	0.02	0.01 ± 0.01	0.01 ± 0.01
^{186}Os	0.01	Undetectable	Undetectable
^{189}Os	0.002	Undetectable	Undetectable

3. Results

3.1. Mass spectrum analysis

The predicted isotopic concentrations were compared to the measured peak concentrations from APT, using the method outlined in previous publications [32]. A total of 6 samples each were used for the single crystal and polycrystalline material, with a total ranged ion count of 1.626×10^7 and 1.371×10^7 respectively. For the polycrystalline material, 2 samples contained a portion of the sub-grain boundary, the other 4 did not.

Mass peak identification and ranging of APT data relies on manual operator input to define the peak width and corresponding element, and is an important source of uncertainty to consider in the reported sample composition [58,59]. Here we apply a under and over raning approach, details of which are given in Appendix A. The standard approach to separating the contributions to an individual mass peak, and correctly labelling the overlapping peaks with the corresponding elements in APT data, is to use the heights of the adjacent non-overlapping mass-to-charge-state peaks to determine the ratio of the elements in the peak. In samples in which transmutation has not occurred, this is possible because the heights of the individual isotopic peaks for an element are distributed according to the natural abundance for that element. In the case of the samples discussed here this approach cannot be used because the Re and Os are introduced "artificially" via neutron reactions with isotopes of W. The predicted distribution of isotopes from FISPACT-II calculations indicate that overlap in mass-to-charge-state peaks corresponding to isotopes of W, Re and Os with equivalent atomic mass number is, in fact, minimal, and allowed peak ranging without deconvolution. This is in contrast to situation in Edmondson et al. [41], where higher transmutation levels in those experiments meant that deconvolution was required.

In general there was good agreement on the Re, Os and Ta concentrations between APT, FISPACT-II and EDX measurements [9] for both samples. The bulk concentration measurments are summarised in Table 1. The single crystal sample had a higher average Re concentration than the polycrystalline by around 0.2 at.%. The concentration of individual isotopes was measured by ranging each mass peak individually and showed also showed a good agreement between the predicted and measured values. The results are summarised in Table 2.

3.2. Precipitation of transmutation products

Precipitation of Re and Os was observed in both single and polycrystalline samples. As demonstrated in Figs. 2–6, both the precip-
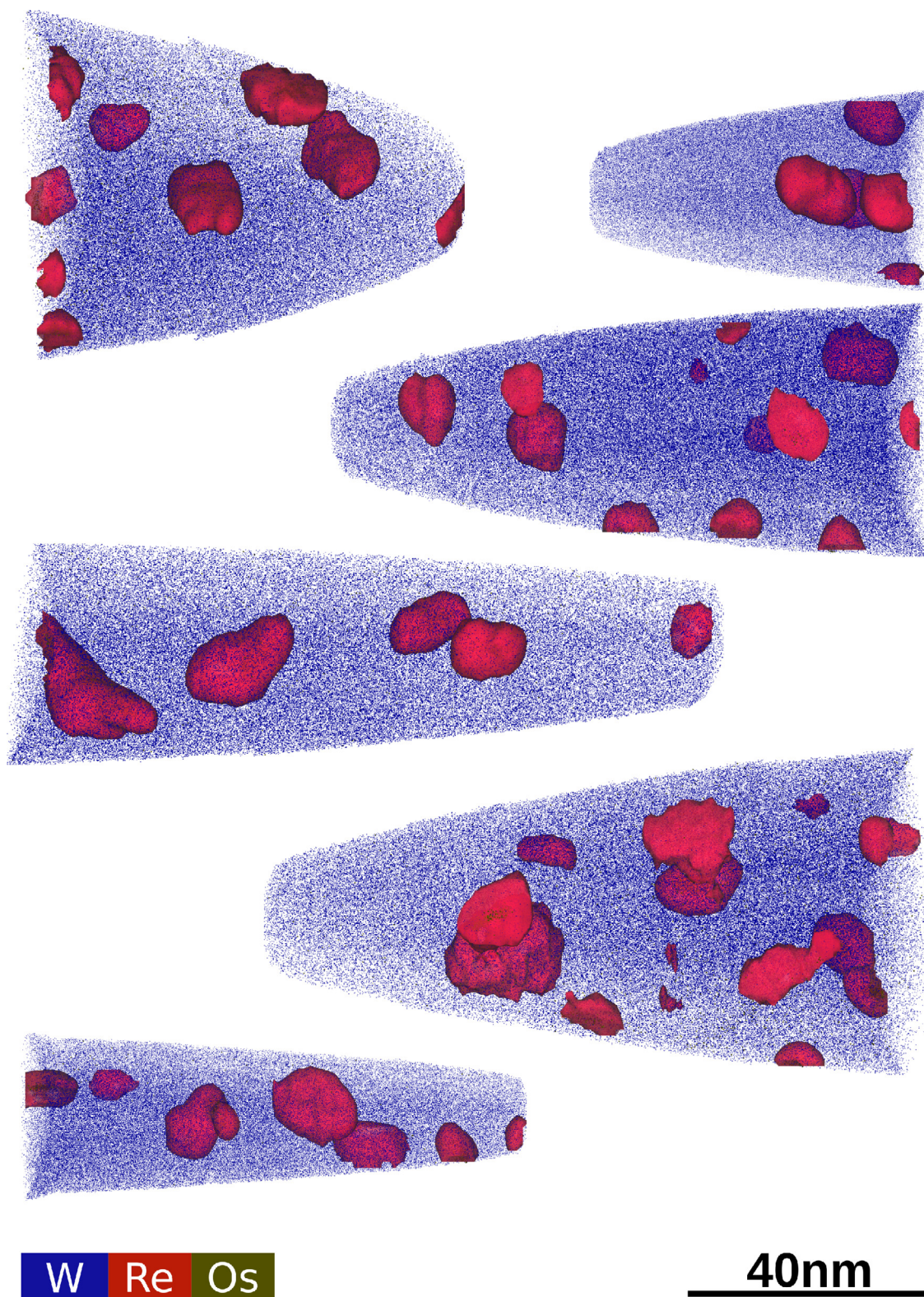
Fig. 2. Summary of the 6 reconstructed APT data sets, taken from the single crystal neutron irradiated sample. W atoms are plotted in blue, with between 5 and 20% of atoms shown for visual clarity. Re isoconcentration surfaces at 5 at.%Re are shown in red to highlight the positions of the precipitates. 100% of Os atoms are plotted in green but are not strongly visible because they are located primarily within the Re clusters. Each atom map shows a different sample analysed using APT. (For interpretation of the references to colour in this figure legend, the reader is referred to the web version of this article.)
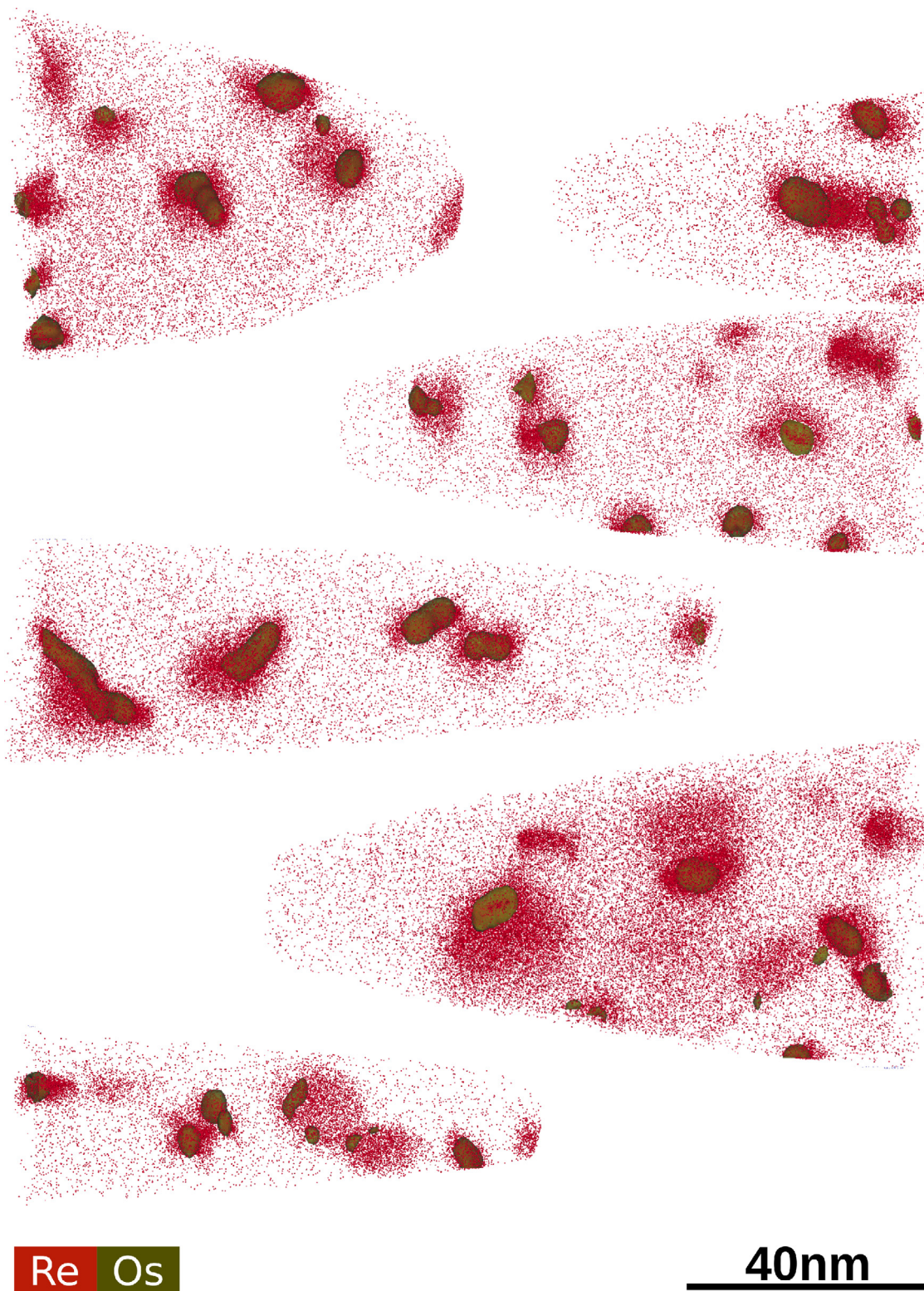
Fig. 3. APT Reconstruction of samples taken from single crystal neutron irradiated sample. Equivalent data to that shown in Fig. 2, however, for visual clarity, only Re atoms (red spheres, 0.1 nm in diameter) are shown, together with Os isoconcentration surfaces at 1.5 at.%. (For interpretation of the references to colour in this figure legend, the reader is referred to the web version of this article.)

itation of Re and Os, as well as the core shell Os structure observed previously has been formed in both single and polycrystalline samples. In this section an overview of the observed clusters is given before further analysis of the compositions is given in Section 3.3.

3.2.1. Single crystal

Fig. 2 shows reconstructions of 6 successful APT needles taken from the single crystal sample. The location of the clusters can be seen by the red isoconcentration surfaces at 5 at.%Re. Ta was present in very small concentrations and was not shown to be correlated with the clusters and
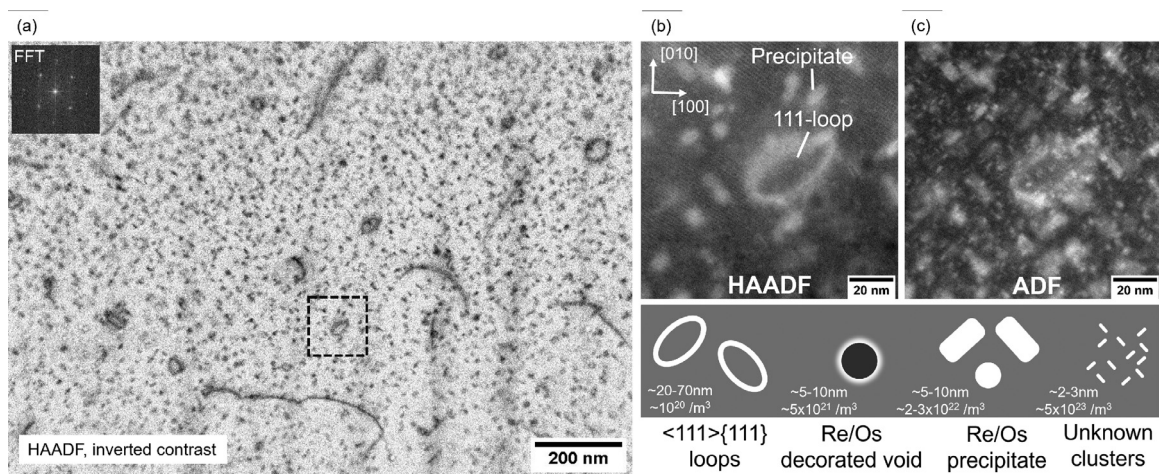
Fig. 4. (a) STEM HAADF image of dislocation loops, voids and Re/Os rich precipitates in the single crystal neutron irradiated sample. Higher magnification image given in (b) shows a ⟨111⟩ dislocation surrounded by Re/Os rich precipitates shown by the contrast in the HAADF and Annular Dark Field (ADF) image in (c). In the lower right is an illustration of the appearance of different features, with the measured number densities. The small unknown features are potentially clusters of Re/Os.
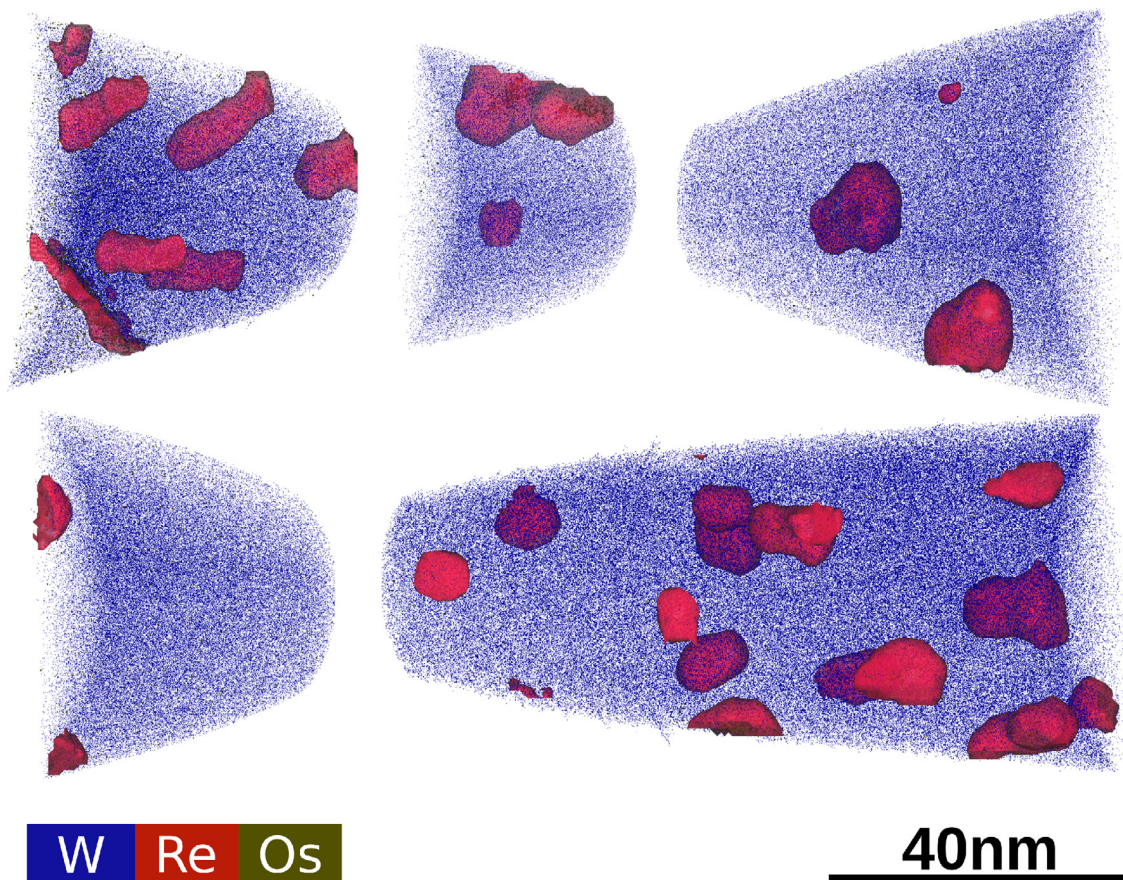

Fig. 5. APT Reconstruction of samples taken from polycrystalline neutron irradiated sample, showing ≈1% of the detected W atoms in blue for visual clarity and red isoconcentration surfaces at 5 at.%Re. (For interpretation of the references to colour in this figure legend, the reader is referred to the web version of this article.)

therefore is not shown in Fig. 2. Large clusters of Re and Os (relative to the reconstruction) were observed in all of the 6 single crystal samples analysed, as shown in Fig. 2. Fig. 3 shows the equivalent data from Fig. 2, with all of the W atoms hidden, and only the Re atoms shown. 100% of the detected Re atoms are plotted, and the location of the Os is highlighted with an iso concentration surface at 1.5 at.%Os.

The map of Os and Re atoms in Fig. 3 clearly shows the strong segregation of these elements. These maps also highlight that Re and Os atoms are not evenly distributed throughout the cluster. The majority of the clusters shown in Fig. 3 have a core which is rich in Re and Os, surrounded by a diffuse cloud of Re, as has been highlighted in other studies [32,40]. The Os isoconcentration surfaces at 1.5 at.%Os indicate
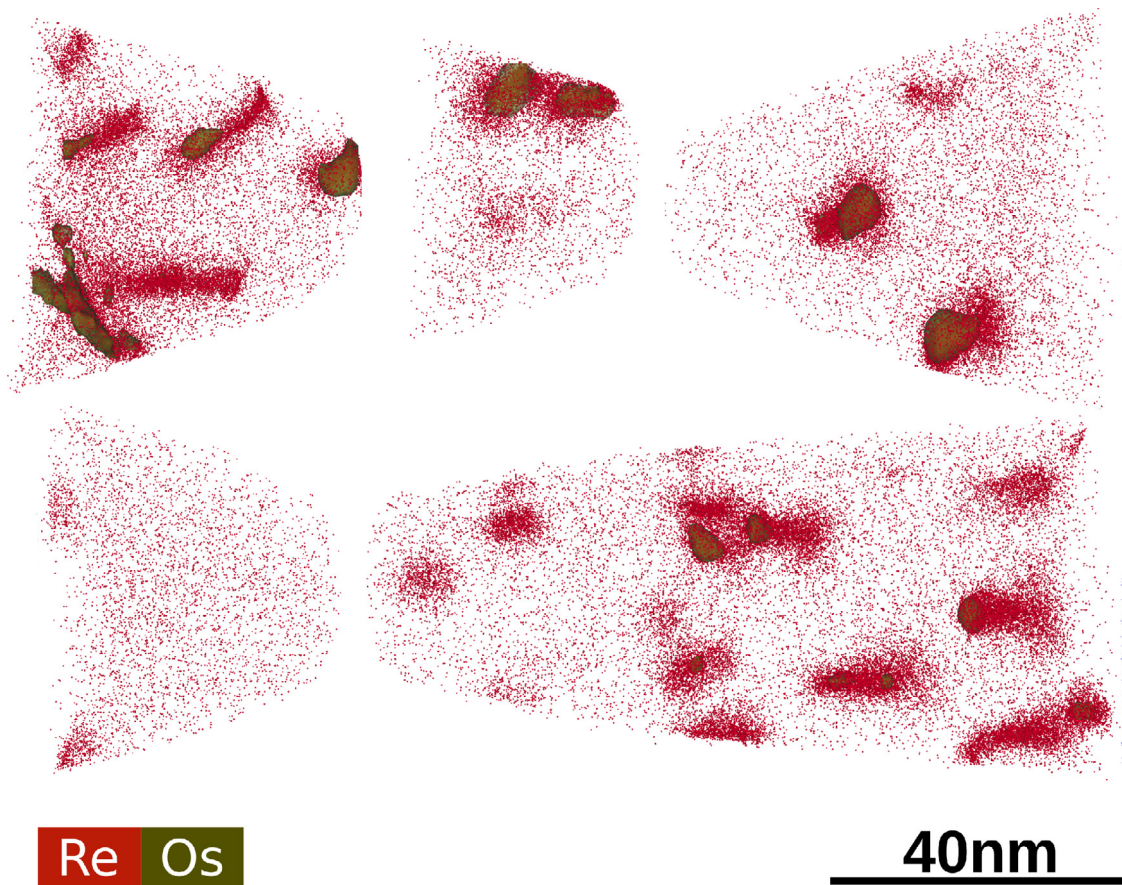
Fig. 6. APT Reconstruction of samples taken from the polycrystalline neutron irradiated sample. Equivalent data to that shown in Fig. 6, however, for visual clarity, only Re atoms (red spheres, 0.1 nm in diameter) are shown, together with green Os isoconcentration surfaces at 1.5 at.%. (For interpretation of the references to colour in this figure legend, the reader is referred to the web version of this article.)

that very strong precipitation of Os has occurred, given that the nominal concentration of Os in the sample is only 0.08 at.% (see Table 1).

HAADF imaging of the single crystal sample also showed the presence of a high number density of Re/Os rich precipitates, as shown in Fig. 4. Re/Os precipitates were identified by their mostly oblong appearance, often with sharp edges and solid contrast, and are visible in both the HAADF and Annular Dark Field (ADF) images shown in Fig. 4. These precipitates were 5–10 nm in length, had a density $2\text{-}3 \times 10^{22}$ m^{-3} and appeared elongated along the $\langle 011 \rangle$ directions.

In the ADF image shown in Fig. 4, a high density of small defects were visible, but are invisible in the corresponding HAADF image. Several of the defects appear needle like in appearance, elongated along $\langle 011 \rangle$ directions. The number density of these small clusters 5×10^{23} m^{-3} and they were typically between 2 and 3 nm in size.

3.2.2. Polycrystalline

Fig. 5 shows the reconstructed samples with between 5 and 20 at.% of the detected W atoms shown in blue, 100 at.% of Os atoms in green, and with 5 at.%Re isoconcentration surfaces shown in red. Fig. 6 shows the same data that is plotted in Fig. 5, with all of the W atoms removed. 100% of the Re atoms are plotted and the location of the Os atoms is highlighted with isoconcentration surfaces at 1.5 at.%Os.

The morphology and structure of the clusters in the polycrystalline material shown in Figs. 5 and 6, are similar to those observed in the single crystal material (Figs. 2 and 3). Large clusters of Re (relative to the size of the reconstruction) can be seen which contain a Re/Os rich core. The segregation of Os is strongest, relative to its low nominal concentration in the sample (0.08 at.% Os). In both samples, the precipitate diameter varied between around 5 and 30 nm, however, some

of the clusters did not have a spherical morphology. Some of the clusters were elongated in one direction, indicating more of a rod shaped morphology.

HAADF imaging of the samples measured a cavity number density of 2.4×10^{22} m^{-3} for the polycrystalline material and 5×10^{21} m^{-3} for the single crystal. Voids were identified from HAADF images, mainly in thicker regions where diffraction contrast is less prominent in the HAADF images. In thinner regions of the crystal, Re/Os segregation around voids is visible via diffraction contrast; in HAADF images as a white halo around a dark centre, and in ADF images by the uniform contrast throughout the void. Voids in the single crystal sample were between 5-10nm in diameter. Previous TEM measurements found cavity number densities of 4.0×10^{21} for the polycrystalline and 2.5×10^{21} for the single crystal material [51]. By comparison, in the reconstructed APT data the number density of Re and Os rich precipitates was measured to be 1.5×10^{23} m^{-3} and 9.65×10^{22} m^{-3} for the polycrystalline and single crystal material respectively.

EDX analysis of these samples in previously published work clearly shows the decoration of voids with Re and Os [32,51]. Atomic density artefacts associated with Re and Os clusters in both of these samples suggests that some of these features within the APT reconstruction were in fact associated with voids. Trajectory focusing aberrations of the ions emitted from the periphery of voids leads to regions of higher than expected atomic density in reconstructed APT data [60,61]. The effect of these features on the reconstructed data is strongly dependant on the material system being studied, the size of the void and the chemical nature of any segregation effects. Furthermore, precipitates with a low field evaporation threshold are expected to result in an increase in the local atomic density during reconstruction, thus it is generally not possi-

Table 3

Number density of different microstructural features measured after neutron irradiation in the single crystal sample using STEM-HAADF and APT. The size of the precipitates in the APT data are defined by the radius of gyration calculated using the maximum speration method outlined in Section 3.3.1. The loop size in the APT data was taken from the single loop shown in Fig. 10.

Feature	HAADF		APT	
	Number density (m^{-3})	Size (nm)	Number density (m^{-3})	Size (nm)
Dislocation Loops	10^{20}	20–70	–	15–20
Voids	5×10^{21}	5–10	–	–
Precipitates	2×10^{22}	5–10	1.5×10^{23}	4.5
Unknown Clusters	5×10^{23}	2–3	–	–

ble to unambiguously distinguish decorated voids and these precipitates in the reconstruction based on associated atomic density artefacts alone.

The number densities of different microstructural features in the single crystal sample are summarised in Table 3. The higher number density of Re and Os rich features in the APT data compared with the STEM analysis suggests that not all of the clusters can be associated with voids. Some of the clusters in the APT data are either isolated, or attached to voids too small to be resolved using STEM. It should be noted that the number density of precipitates measured using APT is based on a very small analysis volume, and some local variations in the precipitate number density are to be expected, particularly in the vicinity of grain boundaries.

Re/Os precipitates were visible in both ADF and HAADF images (see Fig. 4), and appeared also elongated along the $\langle 011 \rangle$ directions. Some precipitates appeared as more circular or square in appearance, similar to the voids, but without a dark centre as would be expected of a Re/Os-decorated void viewed in HAADF. Though one might interpret such a precipitate as being elongated in the view-direction (i.e. along [001]), we can rule this out on the basis that no such precipitates were observed elongated along [010] or [100]. These precipitates were 5–10 nm in length, and had a density $2\text{-}3 \times 10^{22}$ m^{-3}. The average size of the clusters in the APT data was characterised by the radius of gyration, measured using a maximum separation method (the method for which is outlined in Section 3.3.1). In the ADF images (see Fig. 4(c)), a high density of small defects were visible, but invisible in HAADF (Fig. 4(b)). The number density of these unknown clusters was 5×10^{23} m^{-3} and they were typically between 2 and 3 nm in size. The number densities of the different microstructural features imaged in this study using both STEM and APT are summarised in Table 3.

The reconstructions summarised in Figs. 2–6 also contained a small concentration of Ta, as reflected in Table 1. This Ta was also produced during neutron irradiation but via different nuclear reactions to that of Re and Os. Mapping the positions of the Ta atoms showed no visible segregation within the clusters, or any of the other microstructural features analysed in this study such as grain boundaries or dislocations.

3.3. Cluster composition analysis from APT

3.3.1. Maximum separation algorithm

Analysis of the composition of the clusters shown in Figs. 2–6 was first performed using a conventional Maximum Separation Method (MSM) in which an atom is defined to be within in a cluster if the distance between two solute atoms is within a pre-defined separation distance, d_{max}. This is based on the notion that two nearest neighbour solute atoms are more closely seperated within a cluster than if they were to occur in the W matrix. Discrete clusters are defined by creating networks of mutually clustered solute atoms. Additional parameters used for the analysis include the minimum number of ions in a cluster, N_{min}, an envelope distance, L, and an erosion distance, d_e. For further details on the definitions of these parameters the reader is referred to Gault et al. [62]. A maximum separation distance $d_{max} = 1$ nm, an en-

velope parameter, $L = 0.7$ nm, an erosion distance of $d_e = 0.25$ nm and a minimum cluster size of $N_{min} = 20$ ions was used, assuming a cluster core comprised of Re and Os atoms and a matrix of W. These parameters were defined using a combination of visual inspection of the clusters defined in this way, and comparison with previous analyses of ion implanted W-Re samples [16]. Practically, this method was implemented within the posgen [63] program, which is available within the APTTools software package [64].

The average Re/Os concentrations in clusters from the single and polycrystalline samples are summarised in Table 4, with results from experiments at JOYO and HFIR [41,44,65]. The samples have a similar average cluster composition (W-8.6Re-0.6Os for the single crystal and W-6.9Re-0.6Os for the polycrystalline) to the pure-W samples irradiated at JOYO (W-7.6Re-0.2Os), which underwent irradiation with a similar transmutation rate to the HFR samples. The clusters measured in the HFIR sample are on average higher in Re and Os, which can be attributed to the higher transmutation level in that reactor, and the higher nominal post-irradiation Re and Os concentration.

The Re and Os concentration in individual clusters varies significantly with respect to the mean cluster concentration, as shown by the large standard deviations, σ_{Re} and σ_{Os} given in Table 4. Each cluster identified using the MSM is plotted as a black point in Fig. 8, which shows the spread of different cluster compositions that were measured. The cluster compositions vary within a range of $\approx 2\text{-}20$ at.%Re, with Os varying between 0 and 5 at.%.

The composition of the clusters measured using MSM is not consistent with the formation of σ (black region in Fig. 8) or χ phase. In samples irradiated at Joyo to a dose of 0.96 dpa, clusters were also identified in APT data using a MSM. Analysis of the cluster compositions showed that they also did not have a Re and Os concentration that is consistent with the formation of σ phase [44,65].

The cluster composition is highly sensitive to the cluster search parameters, as well as the method used to define the clusters. Another method of measuring the cluster composition is to create isoconcentration surfaces within which the composition is measured. As with the MSM method, the composition measured using a isoconcentration surface depends on how this boundary is defined, and at what composition. To illustrate this, the composition of the clusters in the single crystal sample were measured using Re-Os isoconcentration surfaces at 1.5, 12 and 25 at.%, as shown in Table 4. The average cluster composition given by this method varies between 8.80 at.%Re - 0.61 at.%Os for the 1.5% isoconcentration surface; and 31.66 at.%Re - 6.61 at.%Os for the 25% isoconcentration surface.

Analysis of samples from HFIR using 12 at.%Re-Os isoconcentration surfaces gave an average cluster composition of W-19.62Re - 13.03 Os [41]. A similar Re concentration is seen in the HFR samples studied here (21.13 at.%Re), despite the higher nominal post-irradiation concentration in the HFIR samples (W-6.38Re-3.23Os after 1.8dpa compared to W-1.3Re-0.1Os after 1.67dpa in the samples considered in this study). The level of Os in the HFIR clusters is much higher than in the HFR samples (13.03 at.%Os compared to 6.61 at.%Os respectively). This could

Table 4

Average cluster composition in the single crystal and polycrystalline neutron irradiated samples, measured using various methods. The average composition measured in the sample from JOYO and HFIR were also calculated on APT data using a maximum separation algorithm, details of which are given in Hwang et al. [44]. The samples irradiated at JOYO and HFIR are polycrystalline pure-W and pre-alloyed W-10 at.%Re [65]. The standard deviation of the clusters around the average concentration, σ_x, for the concentration of x is also given, unless marked by a † symbol in which case the value represents the standard error on the mean calculated using $\sigma/\sqrt{N}$, where N is the sample size.

Reactor	Sample	dpa	Analysis method	Re (at.%)	σ_{Re}	Os (at.%)	σ_{Os}
HFR	Pure-W (Single Crystal)	1.67	Maximum Separation	8.6	3.4	0.6	0.6
	Pure-W (Polycrystalline)	1.67	Maximum Separation	6.9	3.6	0.6	0.5
	Pure-W (Single Crystal)	1.67	Line Profile	24.6	12.4	3.4	2.9
	Pure-W (Polycrystalline)	1.67	Line Profile	19.5	6.7	1.8	1.4
	Pure-W (Single Crystal)	1.67	Isoconcentration (1.5 at.%Re-Os)	8.80	4.81	0.61	0.66
	Pure-W (Single Crystal)	1.67	Isoconcentration (12 at.%Re-Os)	21.13	3.90	2.33	0.56
	Pure-W (Single Crystal)	1.67	Isoconcentration (25 at.%Re-Os)	31.66	4.98	6.61	1.60
Joyo	Pure-W [44]	0.96	Maximum Separation	7.6	–	0.2	–
	W-10Re [44]	0.96	Maximum Separation	20.9	–	3.0	–
HFIR	Pure-W [44]	0.90	Maximum Separation	13.4	–	2.6	–
	W-10Re [44]	0.90	Maximum Separation	16.6	–	7.7	–
	Pure-W [41]	0.10	Isoconcentration (1 at.%Re-Os)	11.25	0.83†	0.70	0.08†
	Pure-W [41]	1.80	Isoconcentration (12 at.%Re-Os)	19.62	0.41†	13.03	0.46†

be due to a higher nominal concentration of Os in the HFIR sample, or due to a higher degree of transmutation within the cluster cores due to the lower average neutron energy in the HFIR spectrum.

Fig. 7 (a) and (b) shows a close-up image of a volume extracted from one of the APT data sets shown in Figs. 2 and 3. The volume was extracted using a Re isoconcentration surface at 5 at.%Re, and all of the W atoms are removed for visual clarity. The positions of the Re and Os atoms are plotted separately in red and green respectively. The cluster shown in Fig. 7(a) and (b) has a central rod shaped region surrounded by a cloud of Re. This can be observed in several of the clusters shown in Figs. 2–6. Re-isoconcentration surfaces at 25 at.%Re indicated that in the central rod shaped region of the cluster shown in Fig. 7, the composition is higher than 25 at.%Re. The variation of Re and Os concentration within the clusters were investigated using a line profile analysis technique which is discussed in the following section.

3.3.2. Line profile analysis

Fig. 7 (c) shows the variation in Re and Os concentration along the cluster shown in (a) and (b). The cluster core was first identified using a 25 at.%Re isoconcentration surface and the variation in Re/Os across the cluster was measured using a cylindrical ROI centred on this feature. For each bin, the counting errors exported from IVAS were averaged to give the mean counting error for each of the new bins.

The Re concentration of the cluster shown in Fig. 7 was determined to by <20 at.%Re using the MSM. The corresponding concentration in the central region of this precipitate was measured to be approximately 50 at.%Re using the line profile method. Over the equivalent distance, the Os concentration was around 7 at.%Os. The composition taken at the plateau region of this cluster would place it within the σ phase region of the diagram shown in Fig. 8, whereas the MSM would give a composition within the bcc solid solution region. This is likely due to the MSM incorporating a greater proportion of the Re cloud which surrounds the centre of the precipitates, which has a lower concentration of Re in comparison to the core. To analyse the full set of clusters shown in Figs. 2–6 and automated approach to performing line profile analyses was applied.

3.3.3. Automated line profile analysis

An automated method for performing line profile measurements was used to determine the Re/Os concentration in the centres of the precipitates. The position of the clusters were first identified used a MSM [66] using a d_{max} of 0.7 nm, bulk distance of 0.7 nm, and a N_{min} of 70. The MSM was performed using a modified version of the posgen [63], code patch available as supplementary material. The modification produces line profiles scaled to the radius of gyration of each cluster,

the same method as applied elsewhere [67]. If the cluster radius is r, then the total volume of the line profile is $5.2r^3$, where the length of the line profile parallel to the Z-direction is twice $1.3 \approx \sqrt{\frac{5}{3}}$ above and below the centre of mass of the cluster, and the line profile has a square cross section $\pm\frac{r}{2}$ in both X and Y. This volume is sectioned into 100 bins each with a Z-height of $\frac{5.2r}{100}$. The raw files, one per atom probe volume, are processed by the `processLineProfiles.R` script in R which aggregates all the composition and density line profile data together.

In total 102 clusters were detected and analysed using this method. For each line profile exported using the automated program, a peak detection method was applied in order to generate a measure of the peak concentration. The data was first rebinned into 20 groups with a width of 5 nm to improve counting statistics. The mean of each bin was calculated and the highest 85% of these bin means were selected and averaged. The Os concentration was calculated separately using the same method for each of the Re bins included in this analysis.

The results from the line profile analysis along with the MSM results are plotted in Fig. 8, with the ternary W-Re-Os phase diagram at 1873 K overlaid. The results from the line profile analysis are plotted as circles, with the blue points representing data taken from the single crystal sample and red from the polycrystalline. As was observed using the MSM, the overall Re and Os concentration in the clusters is lower for the polycrystalline sample than the single crystal, as is shown by the average cluster composition given in Table 4. The range of compositions from the line profile analysis is greater than for the MSM, with the maximum cluster composition being reported as 59 at.%Re and 12 at.%Os. The average cluster composition calculated with this method is within the bcc + σ phase region, with some clusters from the single crystal sample within the σ phase region. This indicates that in the centres of some of the precipitates, the threshold composition for σ phase formation may have been reached.

3.4. Dislocation decoration

As shown in Table 3, voids and precipitates had the highest number density, but a smaller quantity of loops were also measured. Fig. 4 shows HAADF and ADF images from a region of the single crystal sample containing several dislocation loops. A single ⟨111⟩ loop is shown in the high magnification HAADF image in (b). The distinction between dislocation loops and Re/Os-precipitate is made challenging due to the fact the latter appear at a high density, and the decoration of Re/Os around dislocation loop cores makes interpretation of g.b = 0 conditions difficult. Because of this, only rough estimates of the number densities of the various microstructural defects are summarised in Table 3, based on their
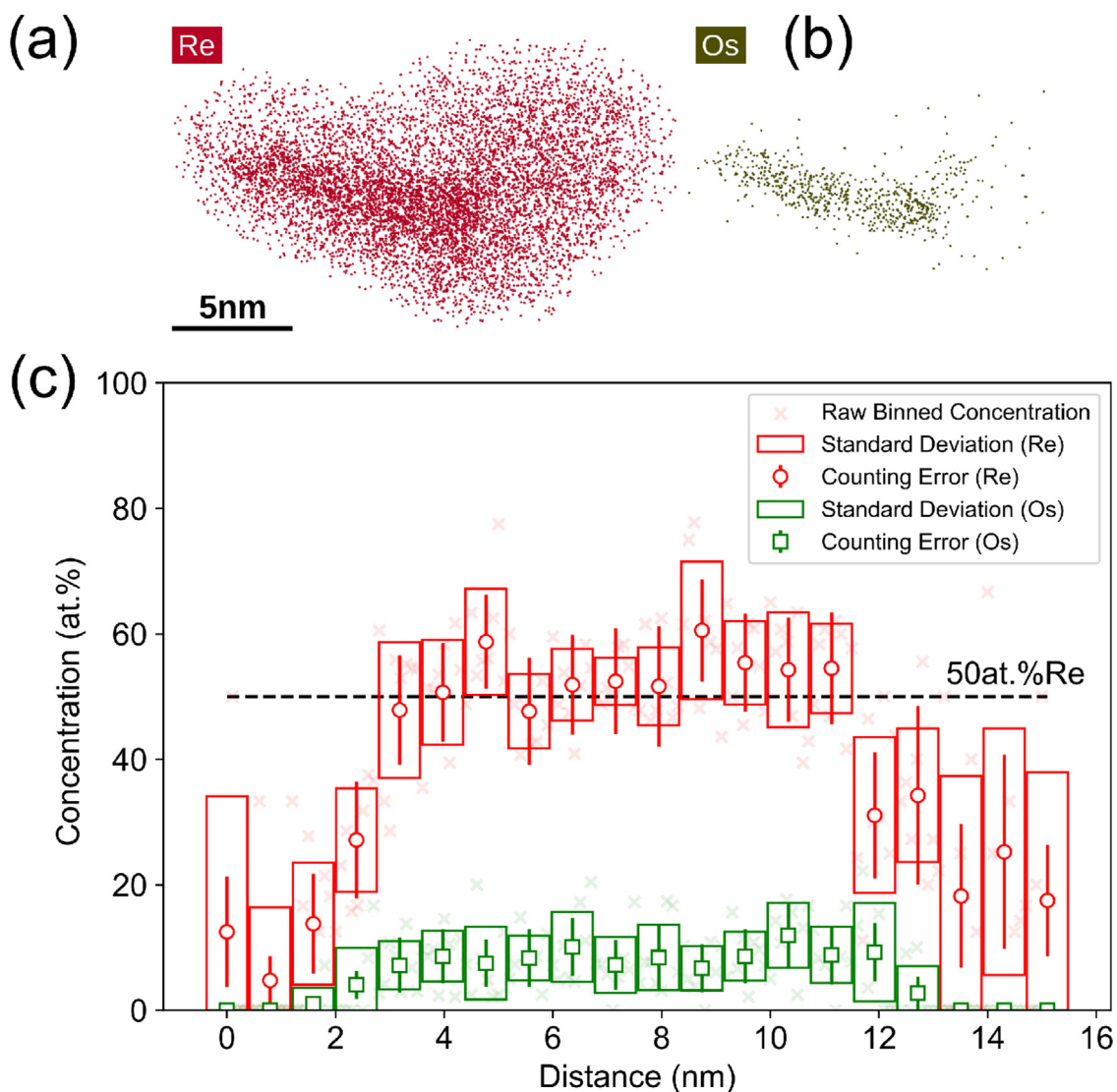
Fig. 7. Shown in (a) and (b) are close-up images of the Re and Os atoms in the precipitate analysed in (c), with atoms plotted as spheres of radius 0.05 nm. 100% of Re and Os atoms are shown respectively with all other atoms hidden for visual clarity. The boundary of the cluster was defined using a 5 at.%Re isoconcentration surface. (c) Line profile taken through rod-shaped cluster in APT data, centred on a 25 at.%Re isoconcentration surface. Cylindrical ROI of dimensions 1.64 nm radius, 15 nm long, binned into 152 bins along the z-direction of width 0.1 nm in IVAS, rebinned into 20 bins. Errors plotted are both counting error from IVAS and the standard deviation on each bin.

appearance in the [100] projection of the foil. Dislocation loops were identified as those defects with a distinctive elliptical-shape. The major axis of the ellipse indicates the likely habit plane; all elliptical loops appeared elongated alone the $\langle 011 \rangle$ directions, as would be expected of pure-edge dislocation loops with Burgers vector $\langle 111 \rangle$. No defects were observed elongated along the $\langle 100 \rangle$ directions, indicating no $\langle 100 \rangle$ dislocation loops were present, nor $\langle 111 \rangle$ loops lying on $\{110\}$ habit planes. The dislocation loops ranged from 20 to 70 nm in size, and had a number density 10^{20} m^{-3}.

Fig. 9 (a) shows one of the APT reconstructions show in Figs. 2 and 3 which was taken from the single crystal material. In Fig. 9(a), 100% of the detected Re atoms are plotted in red and 100% of the detected Os atoms are plotted in green. A line of Os atoms is visible within the highlighted square in Fig. 9(a), which is more clearly highlighted by the 0.5 at.%Os isoconcentration surface in the higher mangnification image shown in Fig. 9(b). Composition line profiles taken perpendicular and parallel to the dislocation are shown in Fig. 9(c) and (d) respectively, which clearly show the segregation of Re and Os to the discloation. Fig. 9(d), which is taken along a ROI orientated along the dislocation

shows a Re concentration of between 4–5 at.%Re and 1–3 at.%Os. This suggests that Os segregates most strongly to dislocations, as the concentration here has increased by over a factor of 10 with respect to the nominal concentration (0.08 at.%) whereas Re has increased by around a factor of 3 from the nominal concentration (1.2 at.%).

Fig. 10(a) shows another APT reconstruction from the single crystal neutron irradiated material, in which 8% of the detected W atoms are plotted in blue and 100% of the Re and Os atoms are plotted separately as red and green spheres respectively. In comparison to the clusters shown in Fig. 7(a) and (b), the central region of the Re rich feature shown in Fig. 10(a) has a more diffuse interface, and is less dense in the core. Furthermore, the Os atoms in Fig. 10(a) are distributed only around the periphery of the Re rich region. As shown in Fig. 10(c), they form a ring around the edge of the Re suggesting that this feature is a dislocation loop. The Os ring is highlighted by the 0.5 at.%Os isoconcentration surface in Fig. 10(b). The size of the feature is consistent with those measured using STEM. STEM imaging of both the single crystal and polycrystalline samples found that the majority of the loops formed within these samples were orientated in the $\langle 111 \rangle$ directions.
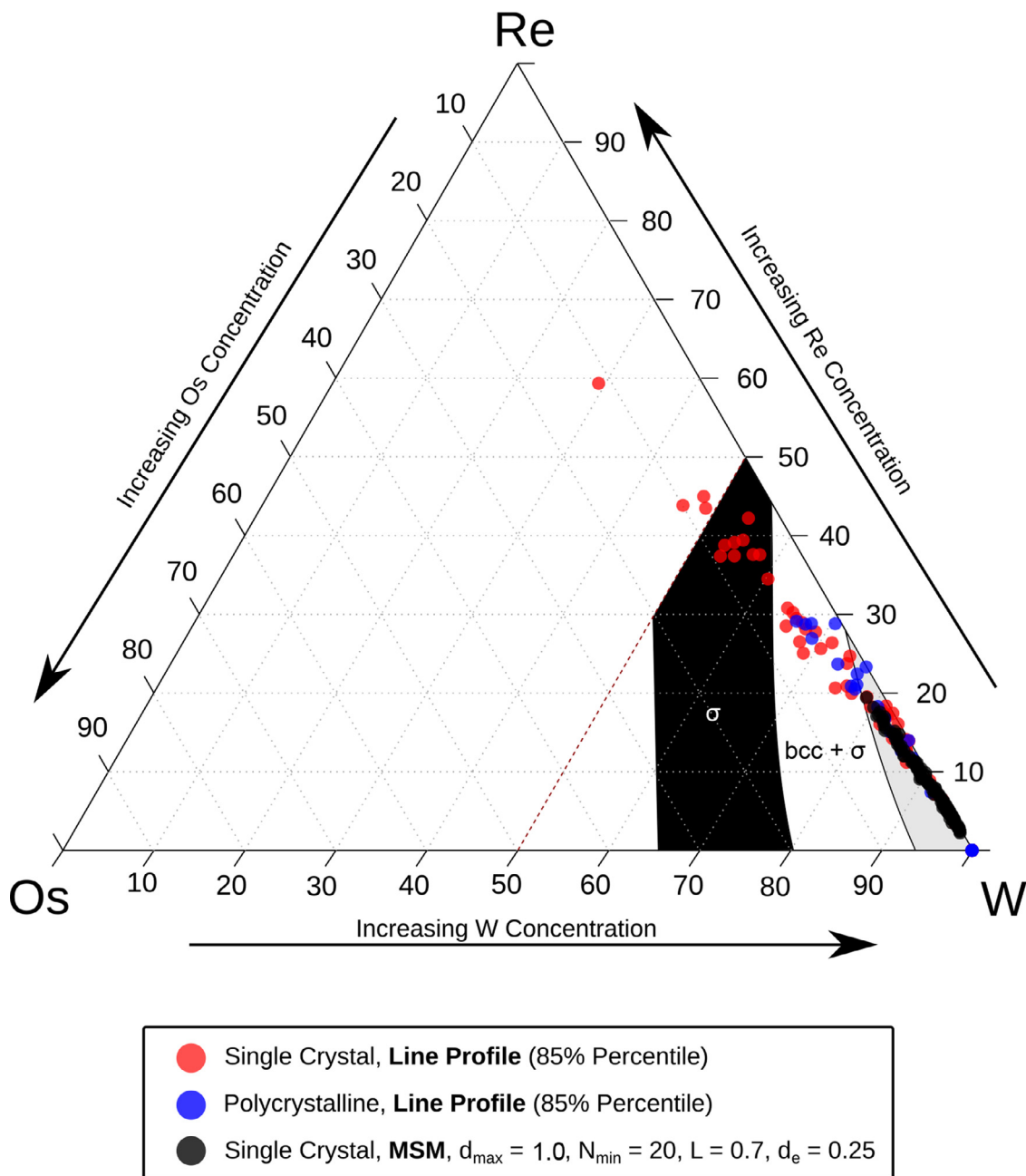
Fig. 8. Partial ternary phase diagram for W-Re-Os at 1873K isotherm, with the region in which σ phase formation is predicted highlighted in black. Overlaid are individual cluster compositions calculated from APT using various methods. The black points were obtained using conventional MSM, whereas the red and blue points were obtained using the line profile analysis method. The red points represent clusters in the single crystal sample, whereas the blue points are cluster from the polycrystalline material. (For interpretation of the references to colour in this figure legend, the reader is referred to the web version of this article.)

Fig. 10 (d) and (e) show line profiles taken using ROIs positioned through the centre of the loop and tangentially to the edge of the loop respectively. In both cases the ROIs were aligned manually with the plane of the Os atoms shown in Fig. 10(c). Fig. 10(d) and (e) show the segregation of Re and Os to the loop. The Re segregation to the loop is stronger than was observed for the line dislocation in Fig. 9, with a central Re composition of between 10 and 12 at.%Re. The two peaks in the Os concentration visible in Fig. 10(d) correspond to the two points at which the ROI crosses the Os isoconcentration surface shown in Fig. 10(b). In the centre of the loop where the Re concentration is highest, no Os atoms are visible. The concentration of Os at the periphery of the loop is measured as between 1 and 4 at.%Os, which is similar to the level observed for the line dislocation in Fig. 9(c) and (d).

3.5. Grain boundary decoration

A reconstruction of the targeted grain boundary APT sample, taken from the polycrystalline material, is shown in Fig. 11(c) and (d). The grain boundary is located centrally within the reconstructed volume and is clearly highlighted by the red Re atoms and green Os atoms. Fig. 11(d) shows the reconstruction rotated by 90 degrees with respect to Fig. 11(c). In the rotated view, there are individual lines of Os atoms visible. The structure within the grain boundary confirms that this is a low angle grain boundary, and that the lines visible in Fig. 11(d) are individual dislocations. Fig. 11(a) and (b) show line profiles taken perpendicular and parallel to, the grain boundary shown in Fig. 11(c). The line profiles were taken using ROIs positioned through the centre of a
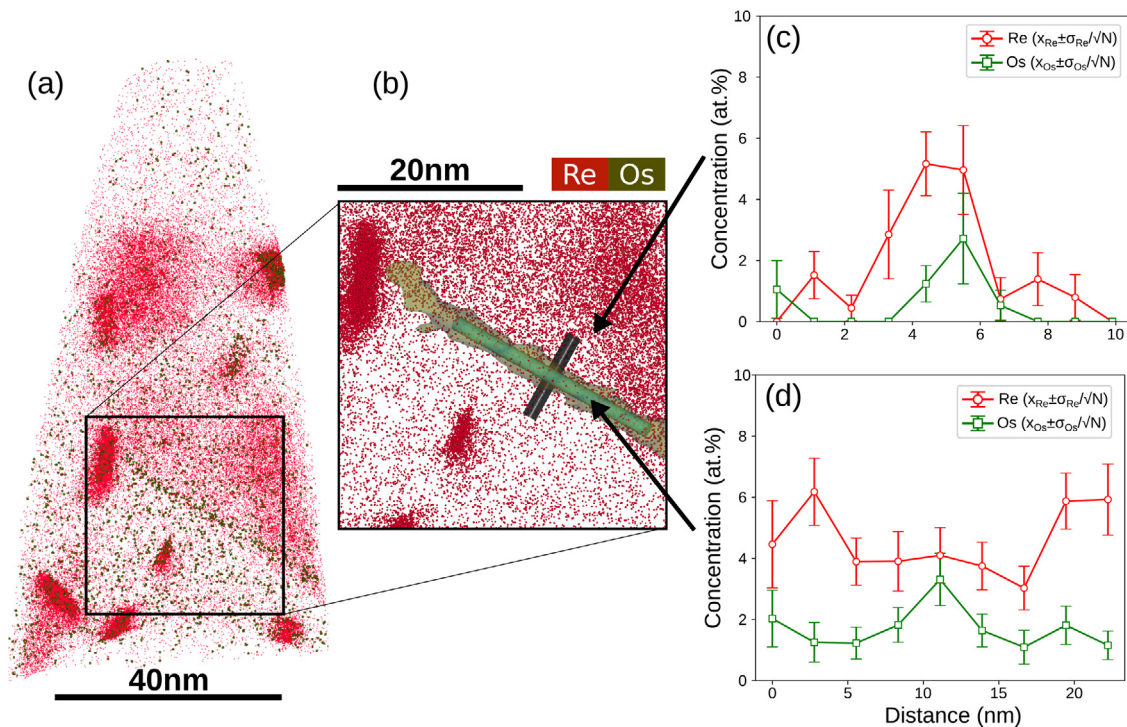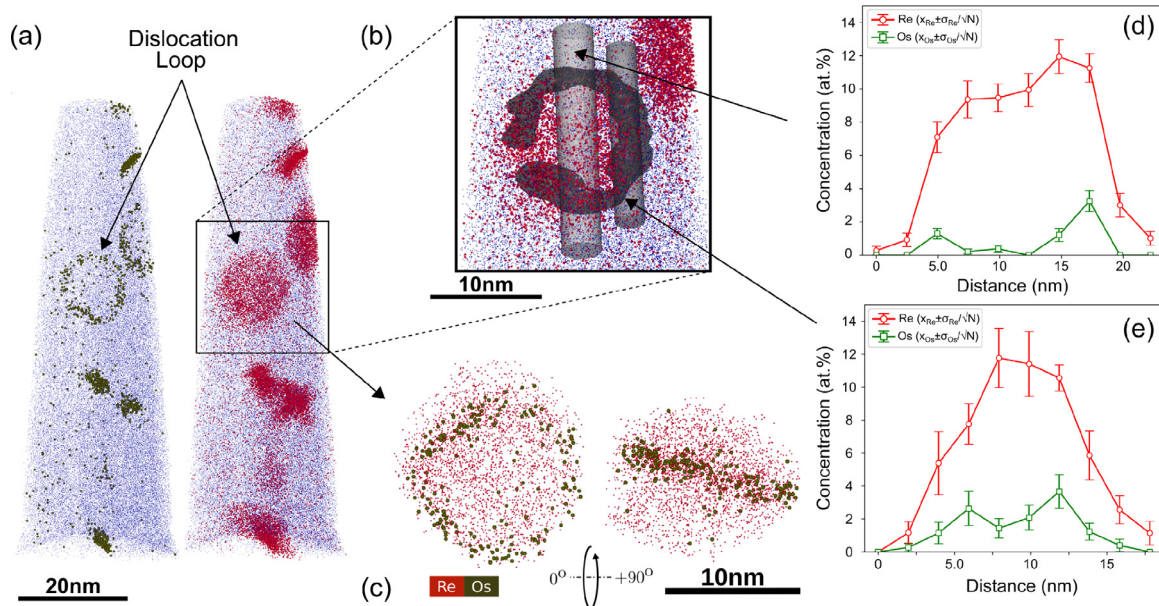
Fig. 9. Segregation of Re and Os transmutation products to a line dislocation in W-1.4Re-0.1Os irradiated to 1.67 dpa at 1173 K, measured using APT. Shown in (a) is the full data set with Re atoms plotted in red and Os atoms in green, with (b) a higher magnification section of the sample with the line dislocation highlighted with a 0.5 at.%Os isoconcentration surface. Plotted in (b) are the ROIs used to analyse the segregation of Re and Os to the disclocation. The plots shown in (c) and (d) show the line profile concentrations from the ROIs shown in (b) for the transverse and in-line directions respectively. In (c) and (d), the circular red points represent Re and the square green points represent Os. The error bar is given by the standard error, $\sigma_{\bar{x}}$ for each of the bins, calculated using $\sigma_{\bar{x}} = \sigma/\sqrt{N}$ where N is the number of points in each bin, and σ is the standard deviation of the bin concentration. (For interpretation of the references to colour in this figure legend, the reader is referred to the web version of this article.)
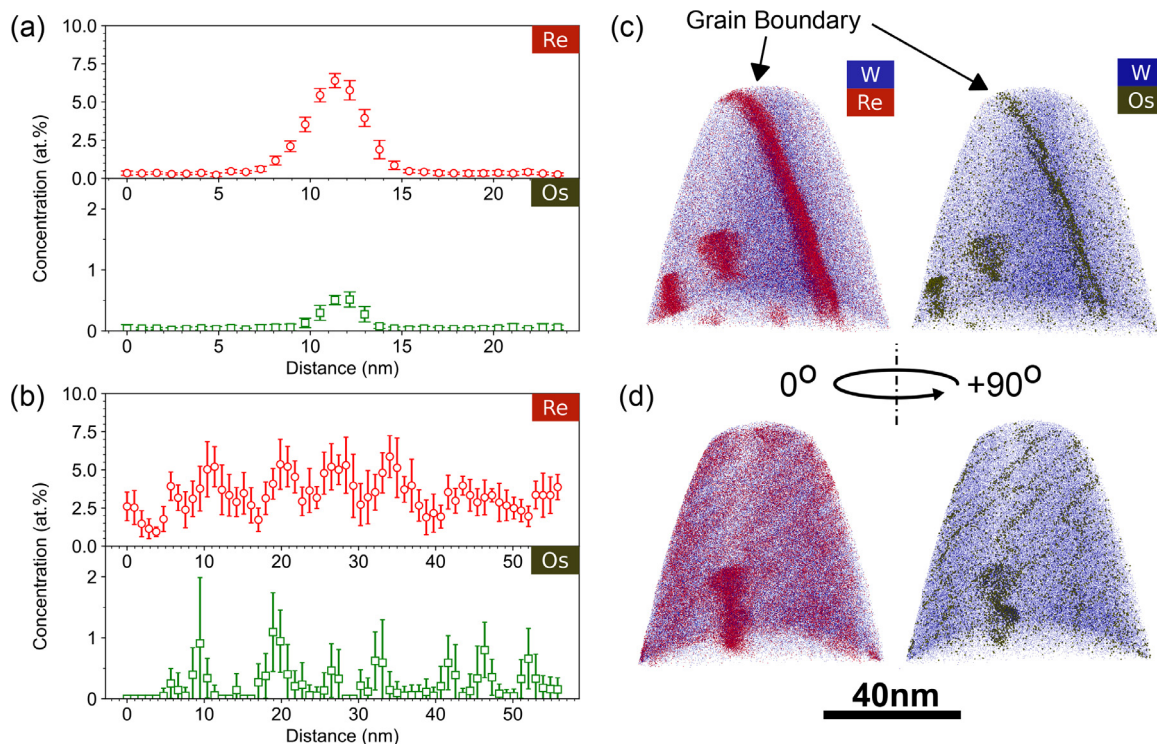

Fig. 10. Segregation of Re and Os transmutation products to a dislocation loop in W-1.4Re-0.1Os irradiated to 1.67 dpa at 1173 K, measured using APT. Shown in (a) is the full reconstructed volume showing 8% of W atoms for visual clarity and Os atoms as green spheres 0.2 nm in diameter, and Re atoms as red spheres of 0.1 nm diameter in order to highlight the respective positions of these atoms. Shown in (b) and (c) are higher magnification views of the loop shown in (a), with the position of the Os atoms highlighted with a 0.5 at.%Os isoconcentration surface in (b) with two cylindrical ROIs defined across the middle of the loop and on the periphery. Shown in (c) is a volume extracted with a Re isoconcentration surface at two different orientations which are rotated 90° with respect to one another, with all W atoms removed. The Re atoms are plotted as small red points and the Os atoms are plotted as spheres of 0.1 nm diameter in order to highlight there position within the volume. Plotted in figures (d) and (e) are the line profile analyses from the central and peripheral ROIs respectively, with Re plotted as red circles and Os plotted as green squares. The error bar is given by the standard error, $\sigma_{\bar{x}}$ for each of the bins, calculated using $\sigma_{\bar{x}} = \sigma/\sqrt{N}$ where N is the number of points in each bin, and σ is the standard deviation of the bin concentration. (For interpretation of the references to colour in this figure legend, the reader is referred to the web version of this article.)

Fig. 11. Decoration of a grain boundary in the polycrystalline neutron irradiated sample, with Re and Os transmutation products. (a) and (b) show line concentration line profiles taken across the grain boundary shown in figures (c), perpendicular to and parallel to the boundary respectively (note that the *x*-axis on (a) and (b) are plotted using different scales). (d) shows the reconstruction in (c), but rotated by 90 degrees. The data was extracted from IVAS in bins of width 0.1 nm, and then re-binned into (a) 30 and (b) 60 concentration bins. The error bar is given by the standard error, $\sigma_{\bar{x}}$ for each of the bins, calculated using $\sigma_{\bar{x}} = \sigma/\sqrt{N}$ where N is the number of points in each bin, and σ is the standard deviation of the bin concentration.

region defined around the boundary using a iso-concentration surface at 1.5 at.%Re. The maximum concentration is between 5–6 at.%Re and 0.5–1 at.%Os. The variation due to individual dislocations within the grain boundary is shown clearly in the parallel line profile in Fig. 11(b).

4. Discussion

4.1. Transmutation product precipitation

The APT measurements of bulk sample compositions summarised in Table 1 show a good agreement with the predicted Re/Os concentrations from FISPACT. The APT samples taken from the polycrystalline sample had a lower overall Re concentration than those taken from the single crystal sample, but this is likely due to the APT samples being taken from the area near to the grain boundary shown in Fig. 11. As shown in Fig. 11, both Re and Os atoms segregate to grain boundaries under irradiation, and the concentration is therefore lower in the samples taken nearby, such as those shown in Figs. 5 and 6, that do not contain a portion of the grain boundary. This highlights the site specific nature of APT and represents an additional source of uncertainty which is not quantified here. In addition to the variation in measured composition due to fluctuations within the sample, changes in the laser pulse energy between APT samples also introduces some smaller variation in the measured composition. Overall however, the bulk measurements support the use of FISPACT-II calculations for assessing post-irradiation sample compositions.

The modelling predicts that mass-to-charge-state overlaps for the irradiation conditions experienced by this sample were minimal due to the short half-lives of the other isotopes formed under irradiation ([185]W and [187]W isotopes have half-lives of 75.1 days and 23.72 hours respectively [3]). Both of these isotopes are produced, during and after irradiation, via transmutation reactions, but do not overlap with the [185]Re

and [187]Re mass-to-charge-state peaks because they decay quickly. Re and Os are produced after irradiation as the unstable precursor isotopes produced during the irradiation decay over time. Because the time between sample removal from the reactor and analysis is several years, the contribution to the [185]Re and [187]Re mass-to-charge-state peaks is minimal. FISPACT-II predicts that [187]Os should account for only 0.01% of the 187 mass peak, with the rest of the counts coming from [187]Re and zero contribution from [187]W. Again with the 185 peak, minimal overlap is predicted with only 3.54×10^{-6}% predicted to arise from isotopes other than [185]Re. There is slight deviation between the predicted and measured [187]Re signal, that could indicate slight inaccuracies in the nuclear data, variation in the local neutron spectrum or because of artefacts in APT.

Precipitates were observed with a Re and Os core shell structure, as seen in previous analyses [32]. The majority of the clusters analysed contained Os, with only a small percentage containing only Re, as shown in Fig. 8. A subset of the precipitates exhibit a rod shaped morphology, with some of the clusters containing an elongated core region. This is unlike the clusters observed under ion irradiation which are typically spherical in morphology [16]. The clusters do not appear as needle shaped as in other APT analyses of neutron irradiated W [40,41]. In the HAADF images shown in Fig. 4 the clusters showed either an oblong or circular shape. The ADF image shown in Fig. 4, also shows a high density of small defects of unknown origin. These defects are invisible in the corresponding HAADF image and are more needle like in appearance, elongated along ⟨011⟩ directions. These are unlikely to be dislocation loops; they have a very different length scale to the larger loops previously identified, and they are unlikely to be loops from FIB damage since the sample was flash-electropolished. If these features were dislocation loops they would be lying close to 110 planes. However, in this case we would also expect to see defects elongated along [100] or [010] since these habit planes would be equally likely. We might also expect good

contrast from small dislocation loops in HAADF, which is closer to the "weak" criterion than ADF (as indicated by the sharp line contrast of the dislocation loop in the HAADF image of Fig. 4), however, these defects are not visible in HAADF image. It is possible that these features could be small Re/Os clusters, however, EDX analysis was unable to confirm this directly. The high number density of Re rich features present in the APT supports the suggestion that these smaller features may be Re/Os clusters.

Decorated voids were observed in the HAADF imaging of the samples. The impact of voids on the APT data was unclear, but the combination of complementary STEM and atomic density measurements in the reconstruction of the APT data suggest that decorated voids are likely to be present in the analysed volume of material. Correlative microscopy with APT and TEM is required to fully understand the impact of voids on the formation of Re and Os rich precipitates in these materials.

Analysis of the cluster compositions using a MSM shows that the precipitates are similar to those observed in other APT analyses of low transmutation rate neutron irradiation experiments, as is reported elsewhere [68]. Analysis shows an average cluster composition of W - 8.5 at.%Re and 0.6 at.%Os, which is well within the solid solution bcc region of the ternary W-Re-Os phase diagram. The cluster compositions are highly variable, as reflected in the standard deviation for the Re and Os cluster composition, which is 3.4 and 0.6 respectively.

The rod shaped core of the precipitates was a denser region of Re and Os rich surrounded by a more diffuse Re cloud, as shown in Fig. 7(a) and (b). Line profile analysis of the central region of the precipitate shown in Fig. 7(a) and (b), plotted in Fig. 7(c), shows that the central region of this precipitate has a composition consistent with σ phase, something that has not been previously reported for this material with APT.

Statistical analysis was performed on the full set of data shown in Figs. 2–6 using a line profile and concentration peak fitting method. The results are summarised in Fig. 8, along with the MSM data. Comparing the data from these different methods, the line profile analysis returned a higher maximum concentration, with one cluster from the single crystal sample having as high as 59 at.%Re and 11 at.%Os. As summarised in Table 4, the average cluster composition reported from the line profile method is considerably higher than with the MSM, at approximately W - 25 at.%Re and 3.4 at.%Os. The data is also more variable, with a larger standard deviation calculated for the line profile method. This is reflected in the data plotted in Fig. 8, where some of the clusters are within the solid solution bcc region of the phase diagram, and others extend well into the σ phase region and beyond. The structure of the clusters, shown in Fig. 7, suggest that the MSM of this material gives an average cluster composition that accounts for both the Re and Os rich core and the diffuse Re cloud around this.

These results highlight that the precipitates are not homogeneous regions of Re and Os. The data shows that in the centre of the precipitates either the formation of σ phase or the onset of σ phase formation has occurred. However, diffraction pattern analysis of these clusters was inconclusive. This is likely due to the small size of the region in which σ phase formation has occurred. This is in contrast to the precipitates analysed in samples from the BR2 reactor by Dürrschnabel et al. [40]. The BR2 samples have similar dose, with a similar transmutation rate at the BR2 reactor (2 dpa, 2 at.%Re, 0.2 at.%Os) but showed a comparatively low number density of voids when compared to the samples presented in this study. The precipitates in the BR2 samples were much larger and more highly concentrated in Re and Os than those discussed in this paper. The reason for the differences are not fully understood but one possibility is that the higher number density of voids provide a higher number density of point defect sinks at which segregation can occur. The W-Re and W-Os mixed interstitial dumbbells are particularly important for the transport of these transmutation products. It is likely that the continued transport of Re and Os to these sinks increase the local concentration until the threshold for σ or χ phase formation is reached. Because of the higher number density of segregation sites in the HFR sample, the level of Re and Os decorating these features af-

ter irradiation is comparatively low, and therefore the concentration at which σ or χ phases can precipitate has not yet been reached.

It is to be expected that the difference in microstructure between the single crystal and polycrystalline samples would have an impact of the post-irradiation microstructure observed using APT and TEM. The presence of grain boundaries in the polycrystalline sample are decorated with transmutation products, as is shown in Fig. 11. In the single crystal sample where no boundaries are present, but the level of transmutation is the same, it would be expected that both voids and clusters would be more enriched in Re/Os. By comparison in the polycrystalline sample grain boundaries remove some of the Re/Os available to segregate to clusters and voids. This is something that can be seen in the comparison of average cluster compositions plotted in Fig. 8. The polycrystalline sample has a high number density of sub-grain boundaries, such as the one imaged in Fig. 11, which are sinks for point defects.

4.2. DFT interpretation of dislocation decoration

Both APT and STEM HAADF was used to show the decoration of dislocation loops with transmutation products. The majority of the loops imaged in the single crystal sample were orientated in the ⟨111⟩ directions. Though it was not possible to directly confirm the nature of these defects from the HAADF images (such as via the inside-outside method), the large void population implies a large population of interstitial defects must be contained somewhere in the microstructure. Given the lack of grain boundaries for interstitials to migrate to, it is reasonable to assume these dislocation loops are interstitial-type. Some curved dislocations were also observed, some of which might be dislocation loops that intercept the foil surface, and some which may be network dislocations that have undergone helical-climb via interactions with interstitial or vacancy defects, and thus may "contain" a proportion of the interstitials, however, this was not confirmed.

The loop was clearly distinguishable from precipitates in the APT data due to the difference in the Re and Os atom distribution. Os atoms formed a ring around the edge of the loop, as shown by the Os isoconcentration surfaces in Fig. 10(b) and atom maps in Fig. 10(c). This agrees with APT studies of W-Os in which Os was found to decorate dislocations in unirradiated W [47]. Re segregation to the dislocations was also observed, but this was not as strong as for the Os relative to the nominal concentration for each element. This highlights that dislocations will act as potential nucleation sites for precipitates.

Fig. 12 shows the binding energy of Ta, Re and Os with a 37 SIA ⟨111⟩ loop in bcc-W versus the distance to the loop center. For all solutes, the interaction inside the loop is either small (below 0.5 eV) or repulsive in the case of Ta. For Os and Re, the interaction becomes meaningful and in fact quite high for Os (1.3 eV) at the loop periphery, i.e. on the last shell of the loop, and more precisely at the corner of the last shell. These are sites which are in compression and the local volume available for the solute is smaller than in the bulk. A similar behaviour had been observed for solutes such as P, Mn, Ni and Si in Fe [69]. Outside the loop, the interaction is attractive but it quickly becomes negligible: the range of the interaction between the solutes and the loop is very short.

For Ta, the interaction remains negligible whatever its position (inside or outside the loop). The trends in the binding energies nicely follow the periodic table: for these three elements, the smaller the atom, the larger the interaction with the loop. Ta atoms being larger than W atoms, are not attracted by the loop, whereas Re and Os which are smaller atoms than W atoms are attracted by the loop. The contribution of the size effect to the interaction is thus non negligible in that case. Fig. 13 shows the binding energy of a single solute atom with the solute for different position of the solute. As already exemplified in Fig. 12, one sees that the interaction is the strongest for the solute at the periphery of the loop and more precisely at the corner of the loop where the strain is the highest. Os is the solute for which the interaction is the highest. Note also that as mentioned in the methodology section, the binding energies are very similar whether calculated with 1 or 2 kpts (See more
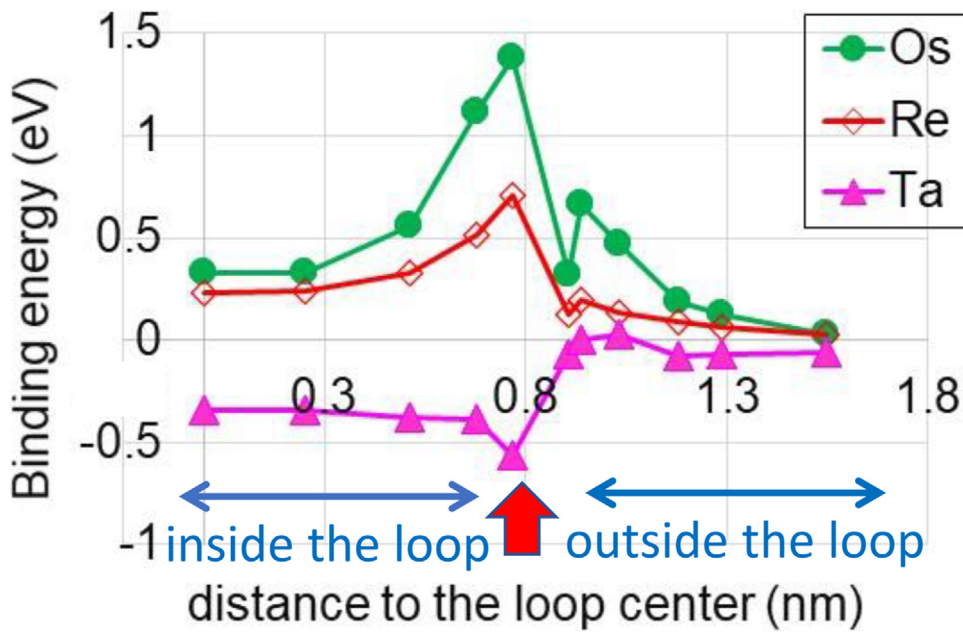
Fig. 12. Plot of the binding energy calculated using DFT with elastic correction between Re, Os and Ta solute atoms within a 37 SIA ⟨111⟩ loop in bcc-W, versus distance to the loop center. The data have been obtained using $2 \times 2 \times 2$ kpoints. The red arrow indicates the loop periphery. Within our reference, a positive binding energy indicates an attractive interaction. (For interpretation of the references to colour in this figure legend, the reader is referred to the web version of this article.)
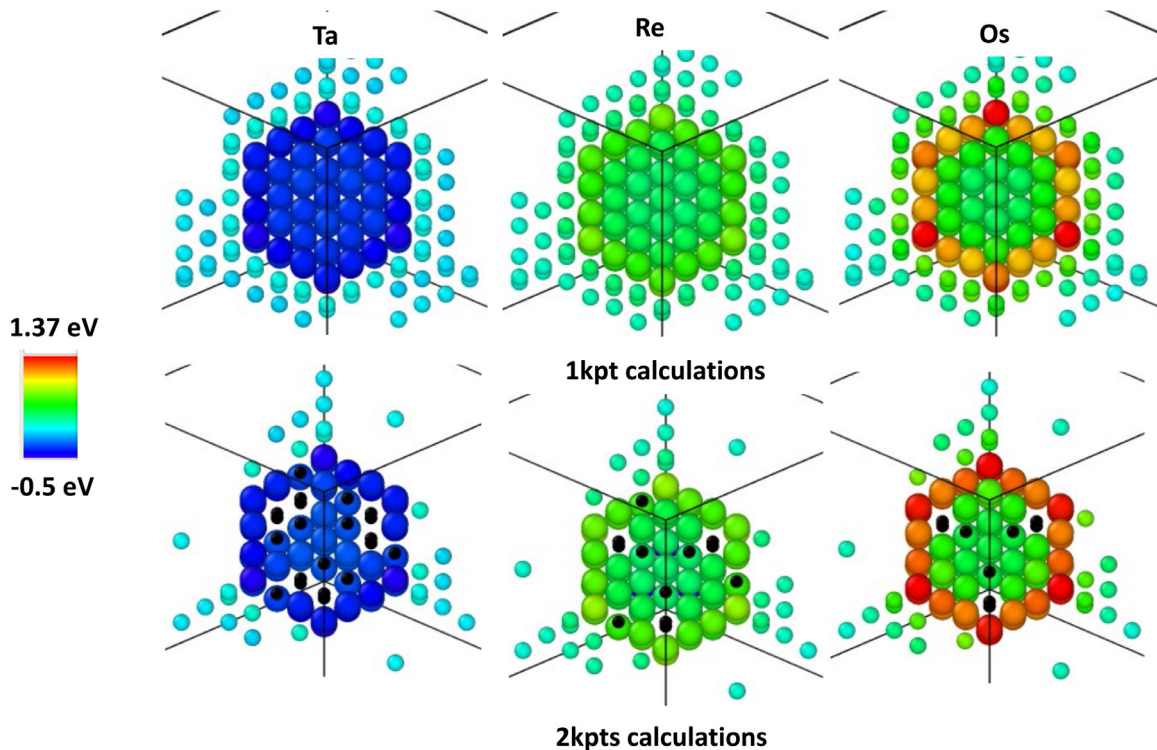

Fig. 13. Binding energy between single Ta, Re or Os solute atoms, with a SIA ⟨111⟩ loop in bcc-W, in various positions. The positions are coloured by their respective binding energy, where a negative binding energy indicates a repulsive interaction. The small black points for the 2 kpts figure represent positions for which the binding energy was not calculated. The atoms of the loops are represented with larger radius.

detailed analysis of binding energy using a different scale for each solute in Appendix.)

The APT results are fully in agreement with the DFT results which indicates that Os atoms have the strongest binding with the loop and that Ta does not bind at all. We propose that the reason Os is mostly seen at the periphery of the loops is because it is the solute species with the strongest interaction with the loop, and because the most stable configuration for solute atoms that bind with the loop is at the periphery. Os atoms therefore occupy these sites at the periphery of the loop preferentially to Re, which binds less strongly. Re atoms are present in larger amounts in the sample and thus are found at the periphery of the loop as well as on other binding sites. Re atoms are therefore found inside the loop, even if there it is less favourable. We checked whether introducing another Re or Os atom in the vicinity of Re or Os atom in the loop for various positions would change the binding energy of the solute with the loop and it just decreases it moderately. Thus within the present study, it seems to be no real co-segregation effect between the two solutes in the loop

It is worth emphasising that the systematic trend of increasing binding energy for the three solute elements interacting with dislocation

loops shown in Figs. 12 and 13 is very consistent with those obtained from both DFT and Monte-Carlo simulations of voids decorated by Ta, Re and Os [70,71]. The presence of both rhenium and osmium inside voids induced by neutron irradiation [32,51] is seen to be sensitive to the concentration of transmutation elements and the correlation between their positions can be interpret in term of short-range order effect between Re and Os [70].

5. Conclusion

This paper summarises the characterisation of high temperature, neutron irradiated W. Neutron irradiation to a dose of 1.67 dpa at 900 °C led to the formation of voids, disclocation loops and Re/Os rich precipitates, with different number densities. Both voids and disclocation loops were decorated with Re and Os. FISPACT-II simulations were generally in good agreement with the measured abundances, both in terms of bulk sample composition and with respect to individual W, Re, Os and Ta isotopes produced via transmutation. This shows that FISPACT can be a reliable and effective means of assessing post-irradiation sample composition in W, provided an accurate description of the neutron energy spectrum is available.

Production of Re and Os under low transmutation rate conditions led to the formation of Re and Os rich precipitates. The segregation of Os to various microstructural features was strongest, relative to its low nominal concentration. The precipitates consisted of a Re/Os rich core, surrounded by a diffuse cloud of Re. The composition in the centre of these was in some cases consistent with σ phase. Automated line profile analysis found that on average the clusters had a composition of 24.6 at.%Re and 0.6 at.%Os, but that the individual cluster composition varied significantly about this mean value.

HAADF imaging of the samples found dislocation loops had formed under irradiation, though with a lower number density than voids and precipitates ($\approx 10^{20}$ m^{-3} for loops compared with 10^{21} m^{-3} for voids). Using APT, dislocation loops were shown to be decorated with Os, and a diffuse cloud of Re. The Os formed a ring around the edge of the loop, with a maximum concentration of ≈ 2 at.%Os. A systematic DFT investigation of interaction between solutes and the SIA $\langle 111 \rangle$ dislocation loop in W demonstrates that Os had the strongest binding energy with the loop in agreement with the present experimental findings.

Low angle grain boundaries were shown to be decorated with both Re and Os transmutation products. Re was present in a higher concentration but the relative increase in the concentration with respect to the bulk composition was highest for Os. A maximum concentration at the grain boundary of between 5–6 at.%Re and 0.5–1 at.%Os was observed.

These observations have important ramifications for the development of W fusion reactor components. In particular, the finding that low nominal Os concentrations can significantly alter the precipitate structure highlights the importance of understanding the early (low transmutant concentration) stages of transmutation in a reactor. It also clearly demonstrates the need for more representative samples, with fusion relevant transmutation rates, to properly understand the competing and synergistic roles of Os and Re in precipitate formation.

Declaration of Competing Interest

The authors declare that they have no known competing financial interests or personal relationships that could have appeared to influence the work reported in this paper.

Acknowledgements

Appendix A. Validation of FISPACT-II results

The post-irradiation composition of the samples was predicted using FISPACT-II nuclear inventory modelling. To validate these calculations, analysis of the APT mass spectrum was performed to measure the chemical composition and isotopic abundance. In total, 6 samples were obtained from the single crystal sample giving a total ion count of 1.626×10^7 ranged ions. For the polycrystalline sample, 2 samples containing a section of the grain boundary were obtained, and 4 without grain boundaries, with a total ion count of 1.371×10^7 ions.

Mass peak identification in APT data relies on manual operator input to define the corresponding element and peak ranging width, and is therefore an important source of uncertainty in the overall sample composition [58,59]. To quantify this uncertainty, two approaches of ranging the mass peaks are applied: one which is defined from background-to-background and another which only accounts for the central part of each mass peak, as outlined in Lloyd et al. [32]. This process was applied to all of the data sets obtained and averaged to give a bulk composition. The reported value for bulk composition of solute component, x, in this study is therefore given by:

$$x = \frac{1}{N} \sum_i^N x_i \pm \frac{|x^i_{\text{over}} - x^i_{\text{under}}|}{2} \tag{1}$$

where x^i_{over} and x^i_{under} refer to the measured composition using the two ranging approaches outlined above, and N is the total number of APT data sets used for analysis.

The averaged bulk compositions from the single and polycrystalline samples are summarised in Table 1, alongside the predictions from FISPACT-II and EDX measurements carried out elsewhere [9]. Overall the measured composition compares well to both EDX [9] and FISPACT-II, with only a slight overestimation in the Re content detected.

The distribution of isotopic abundances was analysed further by creating a range file in which individual isotopes were identified as independent custom defined elements. This file describes the location and width of the region in the mass-to-charge data for which counts are associated with a particular element or ionic species. The same approach to under and over ranging peaks in the mass spectrum data described previously was used to evaluate the uncertainties such that the composition of an isotope is given by Eq. (1). Table 2 shows the isotopic abundances predicted by FISPACT-II modelling as well as the measured abundances in the single and polycrystalline samples from APT (a further 60 + isotopes were predicted by FISPACT in lower concentrations).
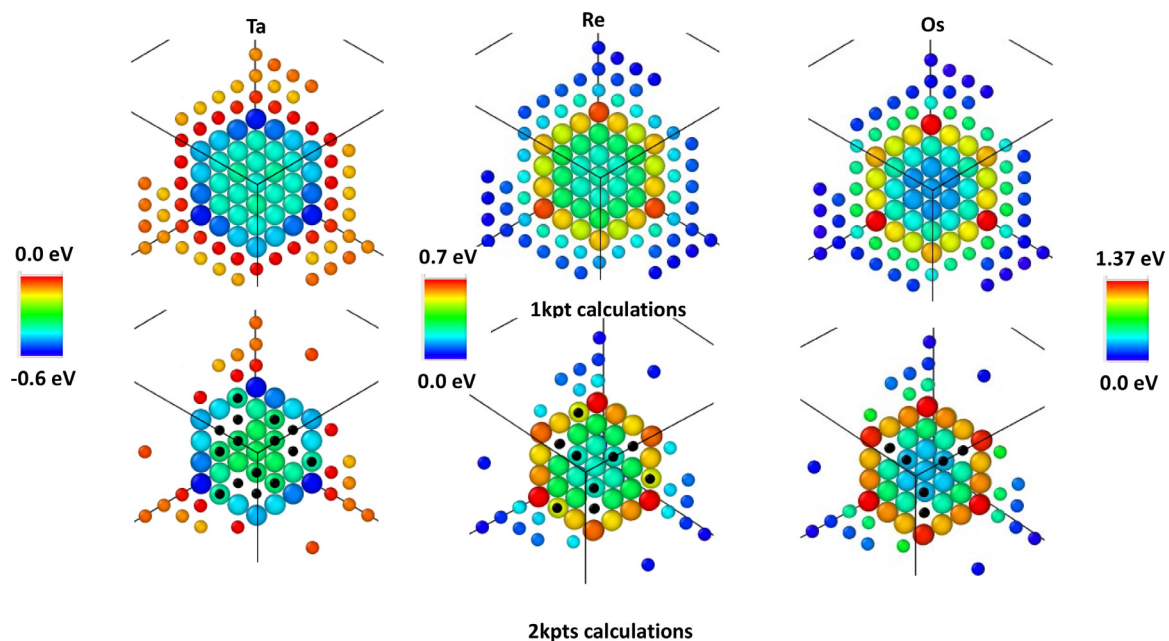
Fig. 14. Binding energy between single Ta, Re or Os solute atoms, with a SIA ⟨111⟩ loop in bcc-W, in various positions, each coloured using a separate scale. The positions are coloured by their respective binding energy, where a negative binding energy indicates a repulsive interaction. The small black points for the 2 kpts figure represent positions for which the binding energy was not calculated. The atoms of the loops are represented with larger radius.

Appendix B. Automated line profile analysis tools for APT data

Included in the supplementary data are the files which make up the patch for the posgen [63] code used to conduct the automated line profile analysis in Section 3.3.3. Included are a range file (WReOsPP.rrng) which defines the mass-to-charge peak labelling, a.xml file used to run posgen [63] and the.txt output files for each of the data sets processed in Section 3.3.3.

Appendix C. Detailed analysis of DFT binding energy for interaction between loops and each of solute elements

Fig. 14 shows the binding energy between a single Ta, Re or Os solute atom with the 37 SIA ⟨111⟩ loop in bcc-W, shown in Fig. 13. In Fig. 14, the colour bar for each solute element is plotted separately, whereas in Fig. 13 all are plotted with the same scale. Fig. 14 shows that for Re, the highest binding energy is at the periphery of the loop, as is the case for Os, but that the Os binding is far stronger than for Re.

Supplementary material

Supplementary material associated with this article can be found, in the online version, at doi:10.1016/j.mtla.2022.101370.

References

[1] Nuclear Energy Agency, Java-based Nuclear Data Information System, 17 February 2019. (Accessed 24 August, 2020) https://www.oecd-nea.org/janis/.

[2] D.A. Brown, M.B. Chadwick, R. Capote, A.C. Kahler, A. Trkov, M.W. Herman, A.A. Sonzogni, Y. Danon, A.D. Carlson, M. Dunn, D.L. Smith, G.M. Hale, G. Arbanas, R. Arcilla, C.R. Bates, B. Beck, B. Becker, F. Brown, R.J. Casperson, J. Conlin, D.E. Cullen, M.-A. Descalle, R. Firestone, T. Gaines, K.H. Guber, A.I. Hawari, J. Holmes, T.D. Johnson, T. Kawano, B.C. Kiedrowski, A.J. Koning, S. Kopecky, L. Leal, J.P. Lestone, C. Lubitz, J.I. Márquez Damián, C.M. Mattoon, E.A. McCutchan, S. Mughabghab, P. Navratil, D. Neudecker, G.P.A. Nobre, G. Noguere, M. Paris, M.T. Pigni, A.J. Plompen, B. Pritychenko, V.G. Pronyaev, D. Roubtsov, D. Rochman, P. Romano, P. Schillebeeckx, S. Simakov, M. Sin, I. Sirakov, B. Sleaford, V. Sobes, E.S. Soukhovitskii, I. Stetcu, P. Talou, I. Thompson, S. van der Marck, L. Welser-Sherrill, D. Wiarda, M. White, J.L. Wormald, R.Q. Wright, M. Zerkle, G. Žerovnik, Y. Zhu, ENDF/B-VIII.0: the 8th major release of the nuclear reaction data library with CIELO-project cross sections, new standards and thermal scattering data, Nucl. Data Sheets 148 (2018) 1–142. Special Issue on Nuclear Reaction Data

[3] M.R. Gilbert, J.-C. Sublet, Handbook of Activation, Transmutation, and Radiation Damage Properties of the Elements Simulated using FISPACT-II and TENDL-2015; Magnetic Fusion Plants, Report No. CCFE-R(16)36, United Kingdom Atomic Energy Authority, Oxford, 2016.

[4] M.R. Gilbert, J.-C. Sublet, Neutron-induced transmutation effects in W and W-alloys in a fusion environment, Nucl. Fusion 51 (4) (2011) 043005.

[5] M.R. Gilbert, T. Eade, T. Rey, R. Vale, C. Bachmann, U. Fischer, N.P. Taylor, Waste implications from minor impurities in European DEMO materials, Nucl. Fusion 59 (2019) 076015, doi:10.1088/1741-4326/ab154e.

[6] D.R. Lide, CRC Handbook of Chemistry and Physics, vol. 85, eighty-fifth ed., CRC Press, Boca Raton, FL, 2005.

[7] T. Tanabe, C. Eamchotchawalit, C. Busabok, S. Taweethavorn, M. Fujitsuka, T. Shikama, Temperature dependence of thermal conductivity in W and W-Re alloys from 300 to 1000 K, Mater. Lett. 57 (19) (2003) 2950–2953.

[8] M.J. Baldwin, R.P. Doerner, Helium induced nanoscopic morphology on tungsten under fusion relevant plasma conditions, Nucl. Fusion 48 (3) (2008) 035001.

[9] R.G. Abernethy, J.S.K.-L. Gibson, A. Giannattasio, J.D. Murphy, O. Wouters, S. Bradnam, L.W. Packer, M.R. Gilbert, M. Klimenkov, M. Rieth, H.-C. Schneider, C.D. Hardie, S.G. Roberts, D.E.J. Armstrong, Effects of neutron irradiation on the brittle to ductile transition in single crystal tungsten, J. Nucl. Mater. 527 (2019) 151799.

[10] P.L. Raffo, Yielding and fracture in tungsten and tungsten-rhenium alloys, J. Less Common Metals 17 (2) (1969) 133–149.

[11] B.G. Butler, J.D. Paramore, J.P. Ligda, C. Ren, Z.Z. Fang, S.C. Middlemas, K.J. Hemker, Mechanisms of deformation and ductility in tungsten—A review, Int. J. Refract. Met. Hard Mater. 75 (2018) 248–261.

[12] A. Gilbert, A fractographic study of tungsten and dilute tungsten-rhenium alloys, J. Less Common Metals 10 (5) (1966) 328–343.

[13] B. Gludovatz, S. Wurster, T. Weingärtner, A. Hoffmann, R. Pippan, Influence of impurities on the fracture behaviour of tungsten, Philos. Mag. 91 (22) (2011) 3006–3020.

[14] E. Gaganidze, A. Chauhan, H.-C. Schneider, D. Terentyev, G. Borghmans, J. Aktaa, Fracture-mechanical properties of neutron irradiated ITER specification tungsten, J. Nucl. Mater. 547 (2021) 152761, doi:10.1016/j.jnucmat.2020.152761. https://www.sciencedirect.com/science/article/pii/S0022311520313696

[15] D.E.J. Armstrong, P.D. Edmondson, S.G. Roberts, Effects of sequential tungsten and helium ion implantation on nano-indentation hardness of tungsten, Appl. Phys. Lett. 102 (25) (2013) 251901.

[16] A. Xu, C. Beck, D.E.J. Armstrong, K. Rajan, G.D.W. Smith, P.A.J. Bagot, S.G. Roberts, Ion-irradiation-induced clustering in W-Re and W-Re-Os alloys: a comparative study using atom probe tomography and nanoindentation measurements, Acta Mater. 87 (2015) 121–127.

[17] A. Xu, D.E.J. Armstrong, C. Beck, M.P. Moody, G.D.W. Smith, P.A.J. Bagot, S.G. Roberts, Ion-irradiation induced clustering in W-Re-Ta, W-Re and W-Ta alloys: an atom probe tomography and nanoindentation study, Acta Mater. 124 (2017) 71–78.

[18] T. Hwang, M. Fukuda, S. Nogami, A. Hasegawa, H. Usami, K. Yabuuchi, K. Ozawa, H. Tanigawa, Effect of self-ion irradiation on hardening and microstructure of tungsten, Nucl. Mater. Energy 9 (2016) 430–435.

[19] Z.X. Zhang, D.S. Chen, W.T. Han, A. Kimura, Irradiation hardening in pure tungsten before and after recrystallization, Fusion Eng. Des. 98 (2015) 2103–2107.

[20] D.E.J. Armstrong, A.J. Wilkinson, S.G. Roberts, Mechanical properties of ion-implanted tungsten–5 wt.% tantalum, Phys. Scr. 2011 (T145) (2011) 014076.

[21] X. Hu, T. Koyanagi, M. Fukuda, Y. Katoh, L.L. Snead, B.D. Wirth, Defect evolution in single crystalline tungsten following low temperature and low dose neutron irradiation, J. Nucl. Mater. 470 (December 2015) (2016) 278–289, doi:10.1016/j.jnucmat.2015.12.040.

[22] A. Hasegawa, M. Fukuda, K. Yabuuchi, S. Nogami, Neutron irradiation effects on the microstructural development of tungsten and tungsten alloys, J. Nucl. Mater. 471 (2016) 175–183.

[23] Y. Katoh, L.L. Snead, L.M. Garrison, X. Hu, T. Koyanagi, C.M. Parish, P.D. Edmondson, M. Fukuda, T. Hwang, T. Tanaka, et al., Response of unalloyed tungsten to mixed spectrum neutrons, J. Nucl. Mater. 520 (2019) 193–207.

[24] J.C. He, G.Y. Tang, A. Hasegawa, K. Abe, Microstructural development and irradiation hardening of w and W-(3–26) wt.% Re alloys after high-temperature neutron irradiation to 0.15 dpa, Nucl. Fusion 46 (11) (2006) 877.

[25] C. Yin, D. Terentyev, A. Dubinko, T. Zhang, M. Wirtz, S. Antusch, R.H. Petrov, T. Pardoen, Impact of neutron irradiation on hardening of baseline and advanced tungsten grades and its link to initial microstructure, Nucl. Fusion 61 (6) (2021) 066012.

[26] L.M. Garrison, Y. Katoh, N.A.P.K. Kumar, Mechanical properties of single-crystal tungsten irradiated in a mixed spectrum fission reactor, J. Nucl. Mater. 518 (2019) 208–225.

[27] F. Hofmann, D.R. Mason, J.K. Eliason, A.A. Maznev, K.A. Nelson, S.L. Dudarev, Non–contact measurement of thermal diffusivity in ion-implanted nuclear materials, Sci. Rep. 5 (2015) 16042.

[28] A. Reza, H. Yu, K. Mizohata, F. Hofmann, Thermal diffusivity degradation and point defect density in self-ion implanted tungsten, Acta Mater. 193 (2020) 270–279.

[29] M.R. Gilbert, J.-C. Sublet, S.L. Dudarev, Spatial heterogeneity of tungsten transmutation in a fusion device, Nucl. Fusion 57 (4) (2017) 044002.

[30] K. Nordlund, S.J. Zinkle, A.E. Sand, F. Granberg, R.S. Averback, R.E. Stoller, T. Suzudo, L. Malerba, F. Banhart, W.J. Weber, W. Francois, S.L. Dudarev, D. Simeone, Primary radiation damage: a review of current understanding and models, J. Nucl. Mater. 512 (2018) 450–479.

[31] K. Nordlund, A.E. Sand, F. Granberg, S.J. Zinkle, R. Stoller, R.S. Averback, T. Suzudo, L. Malerba, F. Banhart, W.J. Weber, F. Willaime, S. Dudarev, D. Simeone, Primary Radiation Damage in Materials: Review of Current Understanding and Proposed New Standard Displacement Damage Model to Incorporate in Cascade Defect Production Efficiency and Mixing Effects, NEA-NSC-DOC–2015-9, Nuclear Energy Agency (NEA) of the Organisation for Economic Cooperation and Development (OECD), Vienna, 2015.

[32] M.J. Lloyd, R.G. Abernethy, M.R. Gilbert, I. Griffiths, P.A.J. Bagot, D. Nguyen-Manh, M.P. Moody, D.E.J. Armstrong, Decoration of voids with rhenium and osmium transmutation products in neutron irradiated single crystal tungsten, Scr. Mater. 173 (2019) 96–100.

[33] M.R. Gilbert, S.L. Dudarev, D. Nguyen-Manh, S. Zheng, L.W. Packer, J.-C. Sublet, Neutron-induced dpa, transmutations, gas production, and helium embrittlement of fusion materials, J. Nucl. Mater. 442 (1–3) (2013) S755–S760.

[34] M.R. Gilbert, T. Eade, C. Bachmann, U. Fischer, N.P. Taylor, Activation, decay heat, and waste classification studies of the European DEMO concept, Nucl. Fusion 57 (4) (2017) 046015.

[35] W.D. Klopp, Review of Ductilizing of Group VIA Elements by Rhenium and Other Solutes, NASA Technical Note, NASA TN D-4955, National Aeronautics and Space Administration, Washington D. C., USA, 1968.

[36] C. Ren, Z.Z. Fang, M. Koopman, B. Butler, J. Paramore, S. Middlemas, Methods for improving ductility of tungsten—A review, Int. J. Refract. Met. Hard Mater. 75 (2018) 170–183.

[37] Y.-J. Hu, M.R. Fellinger, B.G. Butler, Y. Wang, K.A. Darling, L.J. Kecskes, D.R. Trinkle, Z.-K. Liu, Solute-induced solid-solution softening and hardening in bcc tungsten, Acta Mater. 141 (2017) 304–316, doi:10.1016/j.actamat.2017.09.019. http://www.sciencedirect.com/science/article/pii/S1359645417307565

[38] W.D. Klopp, A review of chromium, molybdenum, and tungsten alloys, J. Less Common Metals 42 (3) (1975) 261–278, doi:10.1016/0022-5088(75)90046-6. http://www.sciencedirect.com/science/article/pii/0022508875900466

[39] R.K. Williams, F.W. Wiffen, J. Bentley, J.O. Stiegler, Irradiation induced precipitation in tungsten based, W-Re alloys, Metall. Trans. A 14 (3) (1983) 655–666.

[40] M. Dürrschnabel, M. Klimenkov, U. Jäntsch, M. Rieth, H.C. Schneider, D. Terentyev, New insights into microstructure of neutron-irradiated tungsten, Sci. Rep. 11 (1) (2021) 1–17.

[41] P.D. Edmondson, B. Gault, M.R. Gilbert, An atom probe tomography and inventory calculation examination of second phase precipitates in neutron irradiated single crystal tungsten, Nucl. Fusion 60 (12) (2020) 126013.

[42] J. Rempe, D. Knudson, K. Condie, J. Cole, Long Duration Performance of High Temperature Irradiation Resistant Thermocouples, vol. 4, 2007.

[43] P. Villars, A. Prince, H. Okamoto, Handbook of Ternary Alloy Phase Diagrams: Mg-Ni-P to Y-Zn-Zr, ASM International, Materials Park, OH, USA, 2006.

[44] T. Hwang, A. Hasegawa, K. Tomura, N. Ebisawa, T. Toyama, Y. Nagai, M. Fukuda, T. Miyazawa, T. Tanaka, S. Nogami, Effect of neutron irradiation on rhenium cluster formation in tungsten and tungsten-rhenium alloys, J. Nucl. Mater. 507 (2018) 78–86.

[45] C.-H. Huang, L. Gharaee, Y. Zhao, P. Erhart, J. Marian, Mechanism of nucleation and incipient growth of Re clusters in irradiated W-Re alloys from kinetic Monte Carlo simulations, Phys. Rev. B 96 (9) (2017) 094108.

[46] M.J. Lloyd, R.G. Abernethy, D.E.J. Armstrong, P.A.J. Bagot, M.P. Moody, E. Martinez, D. Nguyen-Manh, Radiation-induced segregation in W-Re: from kinetic Monte Carlo simulations to atom probe tomography experiments, The Eur. Phys. J. B 92 (10) (2019) 241.

[47] H.C. Eaton, H.L. Nordén, The segregation of osmium to grain boundary dislocations in tungsten, Scr. Metall. 17 (8) (1983) 1043–1046.

[48] R. Abernethy, A Thesis Submitted for the Degree of Doctor of Philosophy: Comparison of Ion and Neutron Irradiation of Tungsten for Fusion Applications, Department of Materials, University of Oxford, 2019 Ph.D. thesis.

[49] J.-C. Sublet, J.W. Eastwood, J.G. Morgan, M.R. Gilbert, M. Fleming, W. Arter, FISPACT-II: an advanced simulation system for activation, transmutation and material modelling, Nucl. Data Sheets 139 (2017) 77–137.

[50] A.J. Koning, D. Rochman, J.-C. Sublet, N. Dzysiuk, M. Fleming, S. van der Marck, TENDL: complete nuclear data library for innovative nuclear science and technology, Nucl. Data Sheets 155 (2019) 1–55. Special Issue on Nuclear Reaction Data

[51] M. Klimenkov, U. Jäntsch, M. Rieth, H.C. Schneider, D.E.J. Armstrong, J. Gibson, S.G. Roberts, Effect of neutron irradiation on the microstructure of tungsten, Nucl. Mater. Energy 9 (2016) 480–483.

[52] AtomProbeLab: Matlab-based analysis of Atom Probe Data, 30/06/2016. (accessed 27 August, 2020) https://sourceforge.net/projects/atomprobelab/.

[53] G. Kresse, J. Furthmüller, Efficient iterative schemes for ab initio total-energy calculations using a plane-wave basis set, Phys. Rev. B 54 (1996) 11169–11186, doi:10.1103/PhysRevB.54.11169.

[54] G. Kresse, J. Furthmüller, Efficiency of ab-initio total energy calculations for metals and semiconductors using a plane-wave basis set, Comput. Mater. Sci. 6 (1) (1996) 15–50, doi:10.1016/0927-0256(96)00008-0.

[55] J.P. Perdew, K. Burke, M. Ernzerhof, Generalized gradient approximation made simple, Phys. Rev. Lett. 77 (1996) 3865–3868, doi:10.1103/PhysRevLett.77.3865.

[56] K. Arakawa, M.-C. Marinica, S. Fitzgerald, L. Proville, D. Nguyen-Manh, S.L. Dudarev, P.-W. Ma, T.D. Swinburne, A.M. Goryaeva, T. Yamada, T. Amino, S. Arai, Y. Yamamoto, K. Higuchi, N. Tanaka, H. Yasuda, T. Yasuda, H. Mori, Quantum de–trapping and transport of heavy defects in tungsten, Nat. Mater. 19 (2020) 508–511.

[57] C. Varvenne, F. Bruneval, M.-C. Marinica, E. Clouet, Point defect modeling in materials: coupling ab initio and elasticity approaches, Phys. Rev. B 88 (2013) 134102, doi:10.1103/PhysRevB.88.134102.

[58] D. Haley, P. Choi, D. Raabe, Guided mass spectrum labelling in atom probe tomography, Ultramicroscopy 159 (2015) 338–345.

[59] A.J. London, Quantifying uncertainty from mass-peak overlaps in atom probe microscopy, Microsc. Microanal. 25 (2) (2019) 378–388.

[60] C. Fletcher, M.P. Moody, D. Haley, Towards model-driven reconstruction in atom probe tomography, J. Phys. D: Appl. Phys. 53 (2020) 475303.

[61] X. Wang, C. Hatzoglou, B. Sneed, Z. Fan, W. Guo, K. Jin, D. Chen, H. Bei, Y. Wang, W.J. Weber, Y. Zhang, B. Gault, K.L. More, F. Vurpillot, J.D. Poplawsky, Interpreting nanovoids in atom probe tomography data for accurate local compositional measurements, Nat. Commun. 11 (1) (2020) 1–11.

[62] B. Gault, M.P. Moody, J.M. Cairney, S.P. Ringer, Atom Probe Microscopy, Springer Series in Materials Science, Springer New York, 2012.

[63] D. Haley, Posgen, 2007–2020, (http://apttools.sourceforge.net).

[64] APTTools: A Collection of Utilities for Atom Probe Tomography Analysis, 30-06-2020. (accessed March, 2020), [online] https://sourceforge.net/projects/posgen.apttools.p/.

[65] M. Fukuda, T. Tanno, S. Nogami, A. Hasegawa, Effects of Re content and fabrication process on microstructural changes and hardening in neutron irradiated tungsten, Mater. Trans. 53 (12) (2012) 2145–2150.

[66] J.M. Hyde, C.A. English, Symposium R: microstructural processes in irradiated materials, in: Mater. Res. Soc. Symp. Proc, vol. 650, 2000, p. R6.

[67] A.J. London, S. Lozano-Perez, M.P. Moody, S. Amirthapandian, B.K. Panigrahi, C.S. Sundar, C.R.M. Grovenor, Quantification of oxide particle composition in model oxide dispersion strengthened steel alloys, Ultramicroscopy 159 (2015) 360–367, doi:10.1016/j.ultramic.2015.02.013.

[68] M. Lloyd, A Thesis Submitted for the Degree of Doctor of Philosophy: Radiation Damage and Transmutation in Tungsten, Department of Materials, University of Oxford, 2021 Ph.D. thesis.

[69] C. Domain, C.S. Becquart, Solute - ⟨111⟩ interstitial loop interaction in α-Fe: a DFT study, J. Nucl. Mater. 499 (2018) 582–594, doi:10.1016/j.jnucmat.2017.10.070. https://www.sciencedirect.com/science/article/pii/S0022311517310619

[70] D. Nguyen-Manh, J.S. Wróbel, M. Klimenkov, M.J. Lloyd, L. Messina, S.L. Dudarev, First-principles model for voids decorated by transmutation solutes: short-range order effects and application to neutron irradiated tungsten, Phys. Rev. Mater. 5 (2021) 065401, doi:10.1103/PhysRevMaterials.5.065401.

[71] M.J. Lloyd, E. Martinez, L. Messina, D. Nguyen-Manh, Development of a solute and defect concentration dependant ising model for the study of transmutation induced segregation in neutron irradiated W-(re,os) systems, J. Phys. 33 (2021) 457902, doi:10.1088/1361-648X/ac1ec4.